Investigation of the effect of super-resolution in nonlinear inverse scattering

Vadim A. Markel ●[*]

Department of Radiology, University of Pennsylvania, Philadelphia 19104, USA

The idea that a solution to a nonlinear inverse scattering problem (ISP) can contain information about the target on a subwavelength scale and thus allow one to achieve super-resolution (spatial resolution beyond the diffraction limit) has been around since the 1990s. However, a solid mathematical theory of super-resolution in nonlinear image reconstruction is still lacking. In this paper, we investigate the effect of super-resolution in nonlinear ISPs (both analytically and numerically) by analyzing several inverse problems in which the limit of spatial resolution can be defined precisely. The conclusions we obtain are not optimistic. Although it is possible to create examples of exactly solvable models in which account of nonlinearity in the ISP results in additional mathematically independent equations (one such example is shown herein), our results indicate that super-resolution is not achievable in any practical sense. Rather, we find that the linear subspace of possible solutions to a band-limited linearized ISP is transformed into a more general curved manifold due to the effects of nonlinearity. In the one-dimensional problem with realistic interaction that we have considered, the manifold can have a slightly smaller dimensionality that the subspace of solutions to the linearized problem but it does not contract to a point and the effect is practically insignificant.

I. INTRODUCTION

Achieving the effect of super-resolution is an important goal in imaging, tomography, and signal processing. However, in different fields, the problem is formulated and understood in different ways. In the context of image processing, one is typically interested in deblurring an undersampled or corrupted image by utilizing various *a priori* assumptions [1,2]. This includes such techniques as nonlinear interpolation [3,4], utilization of a prior probability density in the Bayesian framework [5], Laplacian [6,7], total variation [8,9], sparsity-based regularization [10–12], and many variants of the above. A conceptually different group of approaches is to engineer a physical device that can gain access to higher spatial frequencies directly, either by amplifying evanescent waves or by some other means [13,14]. Yet another group of approaches is to use the mathematical structure of the nonlinear inverse scattering problem (ISP) to gain access to the spatial frequencies of the target outside of the conventional band limit [15–19]. The present paper is focused on the latter problem, specifically, in the context of nonlinear inverse scattering. We start by reviewing various ideas that motivate this particular direction in the quest for super-resolved imaging.

It is well known that the spatial resolution that can be obtained by solving the linearized ISP with monochromatic illumination and phase-sensitive detection in the far field is limited to about one-fourth of the wavelength ([20], Sec. 13.1.2). In the above reference, Born and Wolf define the resolution limit as $\lambda/2$ rather than $\lambda/4$, but this is a minor distinction. For three-dimensional tomography, the resolution limit can not be defined precisely but is not smaller than $\lambda/4$ and not larger than $\sqrt{3}\lambda/4$ (see below). Structures on a finer scale can not be resolved in this way. Here we assume monochromatic illumination so that the wavelength is well-defined, and linearization of the ISP can be achieved, for example, by using the first Born approximation.

The band limit of the linearized ISP can be understood as follows. Within the accuracy of the first Born approximation, the scattering amplitude of a three-dimensional object, $f(\mathbf{k}_{in}, \mathbf{k}_{out})$, where $\mathbf{k}_{in}$ and $\mathbf{k}_{out}$ are the incident and outgoing wave vectors, is proportional to $\tilde{V}(\mathbf{k}_{in} - \mathbf{k}_{out})$. Here $V(\mathbf{r})$ is the scattering potential, say, the susceptibility $[\epsilon(\mathbf{r}) - 1]/4\pi$ in the case of electromagnetic scattering, or any other suitable contrast, and

$$\tilde{V}(\mathbf{q}) = \int V(\mathbf{r})e^{i\mathbf{q}\cdot\mathbf{r}}d^3r \tag{1}$$

is the spatial Fourier transform of $V(\mathbf{r})$. Note that we use the notation $\mathbf{k}$, possibly with subscripts, for wave vectors whose length is equal to the free space wave number, that is, $|\mathbf{k}| = k = \omega/c = 2\pi/\lambda$. The notation $\mathbf{q}$ is reserved for a generic Fourier variable whose length is arbitrary.

The scattering amplitude contains all information that is accessible in the far-field scattering experiments. Of course, the contribution of evanescent waves is mathematically nonzero everywhere in space, but it is exponentially small. Given any realistic finite-precision measurements, it can be safely assumed that the measured quantity (in the far field) is the scattering amplitude. Accounting for the fact that $|\mathbf{k}_{in}| = |\mathbf{k}_{out}| = k$, we conclude that the scattering amplitude is not influenced at all by the values of $\tilde{V}(\mathbf{q})$ with $|\mathbf{q}| > 2k$. The region of Fourier space $|\mathbf{q}| < 2k$ is known as the Ewald sphere.

―――――――
[*]vmarkel@upenn.edu

For one-dimensional objects, we can define the resolution limit Δ as the Nyquist sampling rate of a function that is band-limited in the interval of spatial frequencies $[-2k, 2k]$. This leads to the result $\Delta = \pi/2k = \lambda/4$. For three-dimensional objects, the situation is not so simple since the Fourier variable is restricted to a sphere rather than a rectangle, and the standard Fourier analysis does not apply. However, the Ewald sphere can be inscribed inside a cube of the side $4k$. Therefore, Δ is larger than $\lambda/4$ (since not all points inside this cube are accessible to measurements). We can also inscribe a cube of the side $4k/\sqrt{3}$ inside the Ewald sphere. Therefore, Δ is smaller than $\sqrt{3}\lambda/4$ (since some points of the Fourier space outside of this cube are accessible to measurements). In general, we conclude that the resolution limit of three-dimensional tomography satisfies $\lambda/4 < \Delta < \sqrt{3}\lambda/4$. A more precise mathematical statement is that the minimum L_2 norm solution $V^{\mathrm{inv}}(\mathbf{r})$ to the linearized ISP is a spherically low-pass filtered version of the actual potential,

$$
\begin{aligned}
V^{\mathrm{inv}}(\mathbf{r}) &= \int_{|\mathbf{q}|<2k} \tilde{V}(\mathbf{q})e^{-i\mathbf{q}\cdot\mathbf{r}}\frac{d^3q}{(2\pi)^3} \\
&= \int S(\mathbf{r}-\mathbf{r}')V(\mathbf{r}')d^3r',
\end{aligned}
\tag{2a}
$$

where

$$
S(\mathbf{r}) = \frac{\sin(2kr) - 2kr\cos(2kr)}{2\pi^2 r^3}
\tag{2b}
$$

is the point-spread function. This result is based on the assumption that the linearizing approximation is sufficiently accurate and the measurements are ideal and sampled as finely as necessary. If these conditions do not hold, the linearized inverse solution is expected to be less accurate than the low-pass filtered potential defined in (2a). We can say that (2a) is the best possible result one can hope for in the far-field linearized inverse scattering.

Several methods for overcoming the resolution limit of the linearized ISP have been considered in the past. The most straightforward approach is to utilize near-field measurements by using small probes (serving for both illumination and detection) that are placed in the subwavelength vicinity of the imaged object [21–25]. Unfortunately, this technique has several drawbacks, which include a lack of sufficiently simple or reliable models for the probes, the technical difficulty of placing and manipulating the probes in the near-field vicinity of an object, and the exponential decay of the evanescent waves, which renders the associated ISP severely ill-posed. At the same time, direct near-field imaging (that is, mapping the intensity of the near field without solving an inverse problem) is not always meaningful. The problem here is the lack of a strong correlation between the near-field intensity of the scattered field and the geometry of the scattering object [26]. In general, near-field modalities are not useful for deep subsurface tomographic imaging or for imaging of surfaces in the strong multiple-scattering regime.

A large class of methods for obtaining super-resolution is based on utilization of *a priori* information about the target. This approach is applicable to both linear and nonlinear inverse problems. In one example, the prior information concerns the shape of the target [27–29]. In this case,

the inverse problem can be reduced to linear or nonlinear regression. In Ref. [29], the spherical shape prior was used to reconstruct the diameter and the refractive index of a particle from angularly-resolved scattering pattern with deep subwavelength resolution. The method of [29] does not require phase-sensitive measurements but is limited to sufficiently large size parameters since, in the quasistatic limit, the inverse solutions are non-unique. In the case of so-called compositional priors [19,30,31], the medium is assumed to consist of two or more components whose physical properties such as spectra are known but the spatial distribution of the components is not known and must be reconstructed. Typically, compositional priors require multispectral measurements [30,31]. However, they are useful if only monochromatic measurements are available, as was demonstrated in Ref. [19] where $\sim\lambda/10$ spatial resolution in nonlinear inverse electromagnetic scattering was obtained. Generally, the use of prior information is a powerful tool for solving ISPs. However, this tool is applicable in both linear and nonlinear regimes and, in the latter case, the effects of nonlinearity, which are the main subject of this paper, and the effects of accounting for the priors can be conflated. To avoid this possibility, we will assume that no *a priori* information about the target is available.

Another set of methods are based on analytical continuation of $\tilde{V}(\mathbf{q})$ beyond the Ewald sphere. Indeed, if $V(\mathbf{r})$ has a compact support and is sufficiently "nice", then $\tilde{V}(\mathbf{q})$ is an analytical function. Based on this observation, the theorem of global uniqueness of solutions to the ISP can be proved [32]. However, in the practical problems of imaging, $\tilde{V}(\mathbf{q})$ is never known analytically. Rather, it is sampled in a discrete and finite set of points. There is no practical way to extrapolate such measurements beyond the Ewald sphere without making some *a priori* assumptions about the high spatial frequency components of the target. But this is something that we explicitly wish to avoid.

In relation to the above, one important comment can be made. It is widely known that the problem of analytical continuation of a numerically sampled function is severely ill-posed. What is much less appreciated is that the difficulty here is more severe and goes beyond ill-posedness. Numerical data can not be extrapolated without making any unwanted *a priori* assumptions even if the samples could be measured with unlimited numerical precision. Indeed, imagine that y_n ($n = 1, 2, \ldots, N$) is the discrete Fourier transform (DFT) of N variables x_n. If all N "data points" y_n are known, one can stably and uniquely reconstruct all x_n. However, if some of the points y_n are not known (i.e., were not measured), there exists no mathematically reasonable way to guess or predict these quantities unless some additional assumptions on x_n are made. If no such *a priori* information is available, the unknown data points can hold any value and the analyticity arguments or analytical interpolation are of no help in this scenario.

An appealing approach to obtaining super-resolution, which does not rely on *a priori* information about the target or on the analyticity arguments, is to consider and solve a nonlinear ISP. Indeed, the arguments that led us to formulation of the resolution limit are not applicable to nonlinear ISPs. The standard multiple-scattering theory yields the following result

for the scattering amplitude (overall factors are omitted):

$$f(\mathbf{k}_{in}, \mathbf{k}_{out})$$
$$= \int e^{i\mathbf{k}_{in}\cdot\mathbf{r}} V(\mathbf{r}) e^{-i\mathbf{k}_{out}\cdot\mathbf{r}} d^3 r$$
$$+ \int e^{i\mathbf{k}_{in}\cdot\mathbf{r}} V(\mathbf{r}) G(\mathbf{r}, \mathbf{r}') V(\mathbf{r}') e^{-i\mathbf{k}_{out}\cdot\mathbf{r}'} d^3 r d^3 r' + \dots.$$
$$(3)$$

The expression

$$V(\mathbf{r})\delta(\mathbf{r} - \mathbf{r}') + V(\mathbf{r})G(\mathbf{r}, \mathbf{r}')V(\mathbf{r}') + \dots \quad (4)$$

which appears in (3) is the power series expansion of the transfer matrix (T matrix) of the system [33,34], $T(\mathbf{r}, \mathbf{r}')$. Keeping only the first term in the right-hand side of (3) corresponds to the first Born approximation, from which it follows that $f(\mathbf{k}_{in}, \mathbf{k}_{out}) = \tilde{V}(\mathbf{k}_{in} - \mathbf{k}_{out})$ and the resolution limit ensues. However, the second-order term contains Fourier components of V outside of the Ewald sphere. To see this, it is convenient to use the Fourier decomposition of $G(\mathbf{r}, \mathbf{r}')$. In free space, the Green's function depends only on the shift $\mathbf{r} - \mathbf{r}'$ and we can write

$$G(\mathbf{r}, \mathbf{r}') = \int g(\mathbf{q}) e^{i\mathbf{q}\cdot(\mathbf{r}-\mathbf{r}')} d^3 q. \quad (5)$$

With the use of this formula, (3) can be rewritten as

$$f(\mathbf{k}_{in}, \mathbf{k}_{out}) = \tilde{V}(\mathbf{k}_{in} - \mathbf{k}_{out})$$
$$+ \int \tilde{V}(\mathbf{k}_{in} - \mathbf{q}) g(\mathbf{q}) \tilde{V}(\mathbf{q} - \mathbf{k}_{out}) d^3 q + \dots.$$
$$(6)$$

Here $g(\mathbf{q})$ is nonzero in the whole infinite integration domain, except, perhaps, for on some surfaces or lines of zero measure. We thus see that, already to second order, Eq. (6) contains all Fourier components of V. The generic nth order term in the expansion (6) is of the form

$$\int \tilde{V}(\mathbf{k}_{in} - \mathbf{q}_1) g(\mathbf{q}_1) \tilde{V}(\mathbf{q}_1 - \mathbf{q}_2) g(\mathbf{q}_2) \dots$$
$$\times g(\mathbf{q}_n) \tilde{V}(\mathbf{q}_n - \mathbf{k}_{out}) d^3 q_1 \dots d^3 q_n. \quad (7)$$

This integral depends on all Fourier components of V. The logical conclusion seems to be that, beyond the first Born approximation, the scattering data depend on all Fourier components of V and, therefore, solutions to the nonlinear ISPs are not subject to the resolution limit.

The idea that one can break the diffraction limit by solving a nonlinear ISP was put forth in a series of papers by Chew *et al.* [35–38] and then explored by different authors [15–19] and was even the subject of some controversy [39,40]. Overall, the conclusion that accounting for multiple scattering provides information about the Fourier coefficients of the target outside of the Ewald sphere has been largely accepted in physics and engineering communities [41]. The effect is often described in terms of incident propagating waves being coupled inside the sample to evanescent waves by the effects of multiple scattering. Then it is pointed out that evanescent waves carry information about the subwavelength structure of the sample.

There are, however, good reasons to not be convinced. For example, the experimental demonstration of $\sim\lambda/10$ resolution in Ref. [19] is quite striking, but it has been achieved with the use of strong *a priori* information about the target. Some other works operate with the criteria of super-resolution that are not mathematically rigorous. A case in point is the comment [39] on an earlier paper [15] where it is stated that super-resolution can be achieved without any multiple scattering (which is the cause of the ISP nonlinearity) because two noiseless peaks can be visually resolved even if the distance between the two maxima is much smaller than the characteristic width of the peaks. This argument, although in principle correct and easily demonstrable, conflates the problem of detection of a small dip between two peaks with the problem of spatial resolution of images. In general, it is not evident that the previous demonstrations of super-resolution have been afforded by accounting for multiple scattering rather than by some other methods such as using *a priori* information, and it is not evident whether these studies have utilized a mathematically rigorous definition of spatial resolution. The fundamental importance of doing so has been recently highlighted in Ref. [42].

In this paper, we investigate the problem of super-resolution in nonlinear inverse scattering directly by formulating an algebraic nonlinear ISP to which the rigorous criteria of image resolution, i.e., based on the DFT, can be applied. Our conclusion is not optimistic. Briefly, we make the following observation. In the case when the linearized ISP is band limited, all possible solutions to such a linearized ISP form a linear subspace. Account of nonlinearity does not contract this subspace to a point to force a unique solution but rather deforms it into a more general manifold. The dimensionality of this manifold can be somewhat smaller than the dimensionality of the original linear subspace but the effect is practically insignificant. We will explain the reduction of dimensionality by the appearance of additional independent equations, which tend to the trivial identity $0 = 0$ in the linearization limit. The associated perturbation theory is singular in the interaction strength. Numerical simulations presented below indicate that only very few such *statistically significant* additional equations can appear relatively to the total number of unknowns. This does not entail any noticeable improvement of the spatial resolution of reconstructions.

Further, the intersections of the linear subspace of solutions to the linearized ISP with the coordinate planes in the N-dimensional vector space are straight lines. However, the intersections of the manifolds that contain solutions to the nonlinear ISP are more general curves, possibly disconnected. While we can state that any point on a straight line has zero projection onto a line that is perpendicular to the former, the same is not true for the more general curves. In other words, solutions to the nonlinear ISPs may have nonzero Fourier coefficients outside of the band limit but it is not clear whether these (and other) coefficients are correct. Having *some* nonzero Fourier coefficients in the inverse solution outside of the band limit does not necessarily entail super-resolution; to achieve the latter, it is also required that these coefficients be correctly determined. Unfortunately, our results indicate that this is not possible.

We will illustrate the main idea of the paper by using examples of progressively increased complexity and realism. In Sec. II, a general algebraic formulation of the nonlinear ISP will be introduced. A simple exactly-solvable example with three degrees of freedom (unknowns) will be fully analyzed in Sec. III. In the case $N = 3$, the dimensionality of the manifold of solutions to the nonlinear ISP is the same as the dimensionality of the linear subspace of solutions to the linear ISP. However, in the case $N = 4$, an interaction can be devised for which the dimensionality is reduced by 1. The case $N = 4$ with tight-binding interaction can still be solved analytically and is analyzed in Appendix A. An example with N degrees of freedom but a simple unrealistic interaction, which still admits an analytical solution, is analyzed in Sec. IV. Here we show with extensive examples that super-resolution cannot be achieved even though the nonlinear inverse solutions may have nonzero Fourier coefficients outside the linear band limit. We are, however, interested in more realistic interactions, which can be analyzed only numerically. To this end, we introduce in Sec. V a numerical method for determining whether super-resolution can be achieved by solving a nonlinear ISP. The method does not require an explicit solution to the inverse problem and can be applied in a very general setting. In Sec. VI, this approach is used to study a problem with $N = 51^2 = 2601$ degrees of freedom and a realistic interaction. Finally, Sec. VII contains a discussion of obtained results.

II. ALGEBRAIC FORMULATION OF THE NONLINEAR INVERSE PROBLEM

To be solved on a computer, an ISP must be suitably discretized. There are many different ways to affect the discretization. In most cases, discrete orthogonal bases in some relevant functional spaces are introduced. The functions of interest are then approximated by truncated expansions over a finite number of the basis vectors. If the unknown function is approximated by a superposition of N basis vectors, we say that the ISP involves N degrees of freedom. In Ref. [43], a discretization using local voxel-based basis functions was used. Here we prefer to take a slightly different point of view and assume that the degrees of freedom correspond to physical particles rather than voxels in some medium. Each particle will be characterized by a physical parameter called the "polarizability," and the goal of the ISP will be to reconstruct these polarizabilities from a set of external scattering measurements.

The term polarizability was typeset in quotes because it may not always correspond to the electromagnetic polarizability of a particle, which is, by definition, the linear coefficient between the external electric field and the electric dipole moment [44]. In the case of acoustic waves, polarizabilities can also be introduced but they have a different physical interpretation. For example, in Ref. [43], the acoustic polarizability of a voxel was defined. The mathematics, however, in all these physically different scenarios is quite similar, which allows us to consider the problem from a model-independent point of view. In what follows, we will use the terms polarizability, dipole moment, and electric field without quotation marks, keeping in mind that these terms should not be interpreted

literally. In numerical examples, we consider a scalar problem; generalization to vectorial fields of the electromagnetic theory is straightforward but entails a larger computational complexity. Note that the scalar problem that we consider is applicable to the electromagnetic case if all particles lie in a plane and the electric field is polarized orthogonally to this plane (TE polarization). It is is also applicable to acoustic equations in the general 3D geometry.

Consider N small particles located at the points $\mathbf{r}_n$ and characterized by the polarizabilities α_n each, where $n = 1, 2, \ldots, N$. The dipole moment of the nth particle is given by $d_n = \alpha_n E_n$, where E_n is the field at $\mathbf{r}_n$ that is external to the considered particle. This *local* field E_n is a superposition of the *incident* field e_n and the field scattered by all particles except for the nth, that is,

$$E_n = e_n + \sum_{m \neq n} G_{nm} d_m. \tag{8}$$

Here G_{nm} is the *free-space Green's function* with the end points in the centers of the particles n and m and the summation runs over all indexes m except for $m = n$. In what follows, we assume that $G_{nn} = 0$; the particle interaction with itself is included in the polarizabilities α_n. We then arrive at the widely known coupled-dipole equation

$$d_n = \alpha_n \left(e_n + \sum_{m \neq n} G_{nm} d_m \right). \tag{9}$$

Equations of this form have been known and used in physics for a long time, in particular, in the context of the Foldy-Lax approximation [45,46], electromagnetic coupled-dipole approximation [47], discrete-dipole approximation [48,49] (voxel-based discretization of continuous media), etc. A recent review with an emphasis on various definitions of the polarizability α_n is given in Refs. [44,50]. For us, the important point is that all coupled-dipole equations can be written in the form (9).

We can also write (9) in matrix notations as

$$\mathtt{d} = \mathtt{V}(\mathtt{e} + \mathtt{G}\mathtt{d}), \tag{10}$$

where small typewriter-style letters denote vectors, i.e.,

$$\mathtt{d} = \begin{bmatrix} d_1 \\ d_2 \\ \cdots \\ d_N \end{bmatrix}, \quad \mathtt{e} = \begin{bmatrix} e_1 \\ e_2 \\ \cdots \\ e_N \end{bmatrix} \tag{11}$$

are column vectors of the length N. Capital typewrite-style letters will be used to denote matrices. In particular, $\mathtt{V}$ is an $N \times N$ matrix whose elements are

$$V_{nm} = \alpha_n \delta_{nm}. \tag{12}$$

We should keep in mind that $\mathtt{G}$ has zeros on the diagonal, i.e., $G_{nn} = 0$. We will refer to $\mathtt{G}$ as the interaction matrix and to $\mathtt{V}$ as the potential.

The formal solution to (10) is

$$\mathtt{d} = \mathtt{T}[\mathtt{V}]\mathtt{e}, \tag{13}$$

where the functional $\mathtt{T}[\cdot]$ is defined by [33,34]

$$\mathtt{T}[\mathtt{X}] = (\mathtt{I} - \mathtt{X}\mathtt{G})^{-1}\mathtt{X}, \tag{14}$$

and $\mathtt{I}$ is the identity matrix. The *T matrix* $\mathtt{T[V]}$ appearing in (13) is defined by the particle polarizabilities α_n and the interaction matrix elements G_{nm} but is independent of the incident fields e_n. In other words, the T matrix is a property of the scatterer itself and is independent from the illumination and detection schemes.

The field scattered by the target is a linear superposition of the fields scattered by all dipole moments. A single data point, that is, a measurement of the scattered field by the kth detector (or a phased array of detectors) due to the lth incident wave is related to the unknown potential matrix $\mathtt{V}$ by the nonlinear equation

$$(\mathtt{f}_k, \mathtt{T[V]}\mathtt{e}_l) = \phi_{kl}, \tag{15}$$

and $(\mathtt{u}, \mathtt{v}) = \sum_n u_n^* v_n$ denotes the scalar product of two complex vectors. In (15), $\mathtt{e}_l$ is the lth vector of incident fields. We assume that there are N_{in} such distinct vectors, which is equivalent to saying that N_{in} distinct source waves have been used. Similarly, $\mathtt{f}_k$ is the kth vector onto which $\mathtt{d}$ is projected to obtain the kth measurement of the scattered field. There are N_{out} such distinct projections, which corresponds to N_{out} detected scattered waves.

To further simplify the notations, we can rewrite (15) equivalently as

$$\mathtt{AT[V]B} = \Phi, \tag{16}$$

where $\mathtt{A}$ is a $N_{\mathrm{out}} \times N$ matrix whose lines are the line vectors $\mathtt{f}_k^*$ (star denotes Hermitian conjugation) and $\mathtt{B}$ is a $N \times N_{\mathrm{in}}$ matrix whose columns are the column vectors $\mathtt{e}_l$, that is,

$$\mathtt{A} = \begin{bmatrix} \mathtt{f}_1^* \\ \mathtt{f}_2^* \\ \ldots \\ \mathtt{f}_N^* \end{bmatrix}, \quad \mathtt{B} = [\mathtt{e}_1 \quad \mathtt{e}_2 \quad \ldots \quad \mathtt{e}_N]. \tag{17}$$

Note that the size of Φ is $N_{\mathrm{out}} \times N_{\mathrm{in}}$.

Equation (16) gives a general algebraic formulation of a discretized ISP. All ISPs can be brought to this form, assuming only that the underlying physical equations (e.g., Maxwell's equations, Schrodinger equation, acoustic equation, etc.) are linear in the fields. The ISP is stated as follows: given $N_{\mathrm{in}} \times N_{\mathrm{out}}$ measurements (data points) contained in the elements of the data matrix Φ, solve (16) to find the N diagonal elements of the potential matrix $\mathtt{V}$ under the constraint that the off-diagonal elements of $\mathtt{V}$ are zero.

The first Born linearization of (16) is

$$\mathtt{AVB} = \Phi. \tag{18}$$

This equation will be used below for "linearized" inversion. We note that (18) can be obtained from (16) either by setting formally $\mathtt{G} = 0$ or, alternatively, by assuming that $|\mathtt{VG}| \ll |\mathtt{I}|$ in some suitable norm, writing out the power series expansion $\mathtt{T} = \mathtt{V} + \mathtt{VGV} + \mathtt{VGVGV} + \ldots$ and keeping only the first term in this expansion. Unlike the first Born approximation, other linearizing approximations including the first Rytov and the mean-field approximation can not be stated in the operator form but must be written explicitly for the elements T_{nm}.

III. EXAMPLE WITH THREE DEGREES OF FREEDOM

We start with a simple exactly-solvable toy problem, which is nevertheless quite instructive. Consider just three particles with unknown polarizabilities α_1, α_2, and α_3. We further assume that the particles form an equilateral triangle so all pairwise interactions are the same and we can write $G_{12} = G_{23} = G_{13} = g$ (recall that $G_{11} = G_{22} = G_{33} = 0$) so

$$\mathtt{G} = \begin{bmatrix} 0 & g & g \\ g & 0 & g \\ g & g & 0 \end{bmatrix}. \tag{19}$$

In this case, the matrix inverse in (14) can be computed analytically and $\mathtt{T}$ can be expressed in terms of α_n as

$$T_{nm} = \kappa_n \delta_{nm} + g \frac{\kappa_n \kappa_m}{1 - gS}, \tag{20}$$

where

$$\kappa_n = \frac{\alpha_n}{1 + g\alpha_n}, \quad S = \sum_{n=1}^{3} \kappa_n. \tag{21}$$

Equation (20) gives the solution to the forward problem. We now need to formulate the inverse problem, and to this end we need to define the measurement matrices $\mathtt{A}$ and $\mathtt{B}$ that couple the T matrix to the measurements Φ according to (16). We will construct $\mathtt{A}$ and $\mathtt{B}$ using the following basis of mutually orthogonal vectors:

$$\mathtt{u} = \begin{bmatrix} 1 \\ 1 \\ 1 \end{bmatrix}, \quad \mathtt{v} = \begin{bmatrix} 1 \\ -2 \\ 1 \end{bmatrix}, \quad \mathtt{w} = \begin{bmatrix} 1 \\ 0 \\ -1 \end{bmatrix}. \tag{22}$$

Let us assume that the particles are illuminated by two different incident waves, which, up to some overall factors, are given by two of these basis vectors, say, by $\mathtt{u}$ and $\mathtt{v}$ or by $\mathtt{u}$ and $\mathtt{w}$. We will see below that the choice matters. Similarly, the scattered field is measured by two different detectors, which register the projections of $\mathtt{d}$ onto the same two basis vectors. In this case, the measurement matrices $\mathtt{A}$ and $\mathtt{B}$ are transposes [51] of each other so that $\mathtt{AT[V]B} = \mathtt{AT[V]A^T}$ (the upper index $\mathtt{T}$ denotes transposition) is symmetric, and the same must be true for the data matrix Φ, assuming that it is in the range of the forward operator.

We will refer to such data matrices as being *physically admissible*. If a nonsymmetric Φ is measured in an experiment, i.e., due to noise or systematic errors, it is not physically admissible as it does not correspond to any diagonal or even symmetric potential $\mathtt{V}$. If this is the case, one can still seek a solution that fits the data best in some sense. For example, if a noisy nonsymmetric data matrix is measured, one can use the substitution $\Phi \to \frac{1}{2}(\Phi + \Phi^T)$. In this paper, we restrict attention to *ideal* data matrices, which are always in range of the forward operator for some diagonal $\mathtt{V}$.

Note that symmetry is a necessary but not a sufficient condition of physical admissibility of Φ. The sufficient condition is not easy to state in general. Below, we will derive the sufficient and necessary condition for the toy problem at hand; in a more general case, the range of the forward operator can not be easily characterized.

Thus, in the considered setup, there are four measurements (two source waves and two detectors) but only three of them

are independent due to the symmetry of Φ. We therefore conclude that there are only three independent measurements. There are also three unknowns. We are interested whether the linearized ISP has a unique solution and, if it does not, whether accounting for multiple scattering and solving the full nonlinear ISP can fix the ill-posedness and produce a unique solution. We will first consider the case when the linearized ISP is *band-limited* and has no unique solution. Then we will consider the opposite case when the linearized ISP is not band limited. In both cases, we will analyze the solution to the full nonlinear ISP. We will finally discuss why the linearized ISP is band limited in one case but not in the other.

A. Band-limited measurement

Consider the case when the two basis vectors used in the construction of A and B are u and v. Then

$$A = \begin{bmatrix} 1 & 1 & 1 \\ 1 & -2 & 1 \end{bmatrix}, \quad B = \begin{bmatrix} 1 & 1 \\ 1 & -2 \\ 1 & 1 \end{bmatrix}. \quad (23)$$

1. Linearized problem

Let us first analyze the linearized inverse problem. To this end, we use the expressions (23) for A and B, compute the product AVB and substitute this result into (18). This results in the matrix equation

$$\begin{bmatrix} \alpha_1 + \alpha_2 + \alpha_3 & \alpha_1 - 2\alpha_2 + \alpha_3 \\ \alpha_1 - 2\alpha_2 + \alpha_3 & \alpha_1 + 4\alpha_2 + \alpha_3 \end{bmatrix} = \begin{bmatrix} \phi_{11} & \phi_{12} \\ \phi_{21} & \phi_{22} \end{bmatrix}. \quad (24)$$

As noted above, a solution to (24) exists only if $\phi_{12} = \phi_{21}$. However, this is not the only requirement. We note the linear dependence $[1, 4, 1] = 2[1, 1, 1] - [1, -2, 1]$. Therefore, the sufficient and necessary condition of consistency of all equations in (24) is

$$\phi_{12} = \phi_{21}, \quad \phi_{22} = 2\phi_{11} - \phi_{12}. \quad (25)$$

So, only two of the elements of the data matrix Φ are mathematically independent. This already indicates that there are not enough equations in (24) to determine the unknowns uniquely.

Let Φ satisfy the physical admissibility conditions (25). Then (24) is reduced to only two linearly independent equations:

$$\alpha_1 + \alpha_2 + \alpha_3 = \phi_{11}, \quad \alpha_1 - 2\alpha_2 + \alpha_3 = \phi_{12}. \quad (26)$$

Therefore, we can find the projection of $\alpha = [\alpha_1, \alpha_2, \alpha_3]^T$ onto u and v. The projection onto w is fundamentally unknown and cannot be recovered in this setting. If a minimum L_2-norm inverse solution is sought, the unknown projection (w, α) is simply set to zero. We will say that the linearized ISP is *band limited* in such cases. The situation is directly analogous to the case when the unknown Fourier coefficients of a function or a vector are set to zero and the inverse Fourier transform is used to obtain a low-pass filtered reconstruction, i.e., as in (2a).

2. Full nonlinear problem

We now investigate the question whether the band limit will persist in the full nonlinear ISP with the same measurement matrices A and B as above. The T matrix of the

problem with the full account of multiple scattering is given in terms of α_n by (20), and we can use this equation to compute $A T[V] B$. Equating the result of this computation to the matrix Φ (entrywise), we obtain the following equations:

$$\frac{\kappa_1 + \kappa_2 + \kappa_3}{1 - g(\kappa_1 + \kappa_2 + \kappa_3)} = \phi_{11}, \quad (27a)$$

$$\frac{\kappa_1 - 2\kappa_2 + \kappa_3}{1 - g(\kappa_1 + \kappa_2 + \kappa_3)} = \phi_{12}, \quad (27b)$$

$$\frac{\kappa_1 - 2\kappa_2 + \kappa_3}{1 - g(\kappa_1 + \kappa_2 + \kappa_3)} = \phi_{21}, \quad (27c)$$

$$\kappa_1 + 4\kappa_2 + \kappa_3 + \frac{g(\kappa_1 - 2\kappa_2 + \kappa_3)^2}{1 - g(\kappa_1 + \kappa_2 + \kappa_3)} = \phi_{22}. \quad (27d)$$

Note that κ_n are given in terms of α_n by (21). As before, physical admissibility of Φ requires that $\phi_{12} = \phi_{21}$, and there is an additional condition, which we will derive shortly.

Equations (27) can be solved for linear combinations of κ_n's as follows:

$$\kappa_1 + \kappa_2 + \kappa_3 = \frac{\phi_{11}}{1 + g\phi_{11}}, \quad (28a)$$

$$\kappa_1 - 2\kappa_2 + \kappa_3 = \frac{\phi_{12}}{1 + g\phi_{11}}, \quad (28b)$$

$$\kappa_1 + 4\kappa_2 + \kappa_3 = \phi_{22} - \frac{g\phi_{12}^2}{1 + g\phi_{11}}. \quad (28c)$$

Assuming $\phi_{12} = \phi_{21}$, Eqs. (27) and (28) are equivalent. We now recall the linear dependence $[1, 4, 1] = 2[1, 1, 1] - [1, -2, 1]$ and conclude that the rank of the matrix on the left-hand side of (28) is equal to 2. Therefore the necessary and sufficient condition of physical admissibility for (27) is

$$\phi_{12} = \phi_{21}, \quad \phi_{22} = \frac{2\phi_{11} - \phi_{12} + g\phi_{12}^2}{1 + g\phi_{11}}. \quad (29)$$

Note that, in the limit $g \to 0$, the second equation in (29) becomes the same as the second condition for the linearized ISP in (25).

Assuming that Φ is physically admissible, the whole set (28) is equivalent to the two equations (28a) and (28b). We thus see that the solution to the nonlinear ISP is band limited if we view κ_n's as the unknowns. But it is not band limited with respect to α_n's. To be sure, the solution for α_n's is still not unique. However, it is not possible to talk about a band limit for α_n's since the set of solutions that are consistent with (28a) and (28b) is no longer a linear subspace but, rather, a curved manifold. In the simple case considered here, this manifold is a two-dimensional surface in the three dimensional space. Intersection of this surface with the plane $\alpha_2 = \text{const}$ are the curves defined by the equation

$$\frac{\alpha_1}{1 + g\alpha_1} + \frac{\alpha_3}{1 + g\alpha_3} = \frac{1}{3} \frac{2\phi_{11} + \phi_{12}}{1 + g\phi_{11}}, \quad (30a)$$

and α_2 can be reconstructed uniquely as

$$\alpha_2 = \frac{\phi_{11} - \phi_{12}}{3 + g(2\phi_{11} + \phi_{12})}. \quad (30b)$$

In fact, (30) defines a union of two disjoint manifolds. The loci of all points in the (α_1, α_3) plane that satisfy (30)
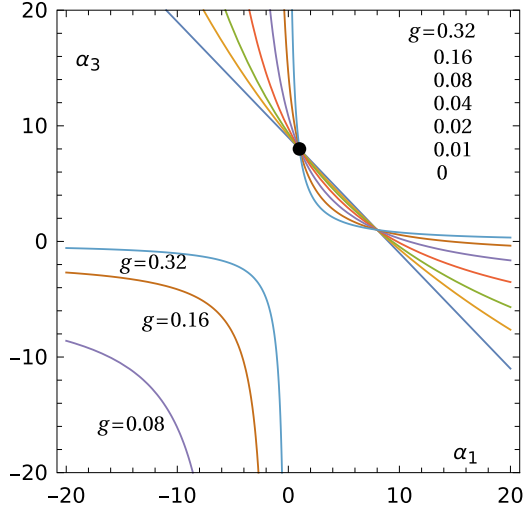
FIG. 1. Loci of all points in the (α_1, α_3) plane that satisfy (30) for different values of the coupling parameter g, as labeled. The data matrix Φ was generated (for each value of g) by using the following model values of the polarizabilities: $\alpha_1^{\text{mod}} = 1$, $\alpha_3^{\text{mod}} = 8$; this point is shown by the black dot. Every curve, except for the one with $g = 0$, consists of two disjoint segments. One of these two segments contains the model point and the other does not. The segments of the curves $g = 0.01, 0.02, 0.04$ that do not contain the model point lie outside of the figure frame.

are illustrated in Fig. 1. It can be seen that the account of nonlinearity does not make the ISP any better posed and does not provide additional information. Rather, characterization of solutions becomes more complicated. Whereas, in the linear regime, the projection of the solution onto a linear subspace (in this case, of $\mathbb{R}^3$) is known from the data, there is no such simple consideration in the nonlinear case.

One can also observe that, if an initial or an intermediate guess in some optimization procedure happens to lie on the "remote" manifold of possible solutions (the one that does not contain the true solution), then there is little hope that any iterative process will converge to the correct result regardless of the regularization method.

B. Measurement without a band limit

As mentioned above, the choice of the basis vectors for construction of the measurement matrices A and B matters. In Sec. III A, we used $\mathtt{u}$ and $\mathtt{v}$ to this end. Let us now use $\mathtt{u}$ and $\mathtt{w}$. Then

$$A = \begin{bmatrix} 1 & 1 & 1 \\ 1 & 0 & -1 \end{bmatrix}, \quad B = \begin{bmatrix} 1 & 1 \\ 1 & 0 \\ 1 & -1 \end{bmatrix}. \tag{31}$$

We will see that in this case the inverse problem is not band limited.

1. Linearized problem

The linearized problem for the measurement matrices A and B defined in (31) takes the form

$$\begin{bmatrix} \alpha_1 + \alpha_2 + \alpha_3 & \alpha_1 - \alpha_3 \\ \alpha_1 - \alpha_3 & \alpha_1 + \alpha_3 \end{bmatrix} = \begin{bmatrix} \phi_{11} & \phi_{12} \\ \phi_{21} & \phi_{22} \end{bmatrix}. \tag{32}$$

It can be seen that the necessary and sufficient requirement of physical admissibility of the Φ matrix is its symmetry; there are no other conditions. Consequently, (32) contains three independent linear equations whose unique solution is

$$\alpha_1^{\text{inv}} = \tfrac{1}{2}(\phi_{22} + \phi_{12}), \tag{33}$$

$$\alpha_2^{\text{inv}} = \phi_{11} - \phi_{22}, \tag{34}$$

$$\alpha_3^{\text{inv}} = \tfrac{1}{2}(\phi_{22} - \phi_{12}). \tag{35}$$

Therefore, the linearized inverse problem in this case is well posed and not band limited.

2. Full nonlinear problem

The full nonlinear problem for the chosen measurement matrices A and B is given by the following four equations:

$$\frac{\kappa_1 + \kappa_2 + \kappa_3}{1 - g(\kappa_1 + \kappa_2 + \kappa_3)} = \phi_{11}, \tag{36a}$$

$$\frac{\kappa_1 - \kappa_3}{1 - g(\kappa_1 + \kappa_2 + \kappa_3)} = \phi_{12}, \tag{36b}$$

$$\frac{\kappa_1 - \kappa_3}{1 - g(\kappa_1 + \kappa_2 + \kappa_3)} = \phi_{21}, \tag{36c}$$

$$\kappa_1 + \kappa_3 + \frac{g(\kappa_1 - \kappa_3)^2}{1 - g(\kappa_1 + \kappa_2 + \kappa_3)} = \phi_{22}. \tag{36d}$$

Just like in the linearized case, the only condition of physical admissibility of the Φ-matrix is its symmetry. Assuming this condition holds, (36) has the following unique solution for κ_n:

$$\kappa_1^{\text{inv}} = \frac{1}{2}\left(\phi_{22} + \phi_{12}\frac{1 - g\phi_{12}}{1 + g\phi_{11}}\right), \tag{37a}$$

$$\kappa_2^{\text{inv}} = -\phi_{22} + \frac{\phi_{11} + g\phi_{12}^2}{1 + g\phi_{11}}, \tag{37b}$$

$$\kappa_3^{\text{inv}} = \frac{1}{2}\left(\phi_{22} - \phi_{12}\frac{1 + g\phi_{12}}{1 + g\phi_{11}}\right). \tag{37c}$$

From (37), one can find α_n as $\alpha_n^{\text{inv}} = \kappa_n^{\text{inv}}/(1 - g\kappa_n^{\text{inv}})$. If we set $g = 0$, (37) becomes equivalent to (36).

We thus see that if the solution to the linearized problem is unique, it remains unique in the full nonlinear case. Indeed, if we fix the data (e.g., assuming that they were measured experimentally) and increase the interaction parameter g in (37), the solution will start off as the linearized solution (33) and remain unique except at the point of discontinuity $g = -1/\phi_{12}$; no bifurcations of the solution will occur.

Another way to analyze the inverse solutions is to fix g (assuming it is known theoretically) and to consider the dependence of α_n on the elements of the data matrix Φ. For sufficiently small Φ, this dependence is linear and given by (33). This means that when the data matrix is sufficiently small (for a given g), the linearized solution to the ISP is accurate. As Φ increases, the nonlinearity sets in and, eventually, the inverse solutions experience discontinuities. This is illustrated in Fig. 2. The presence of discontinuities is the main feature that distinguishes the solution to the nonlinear ISP from its linearized counterpart. If the data is close to the
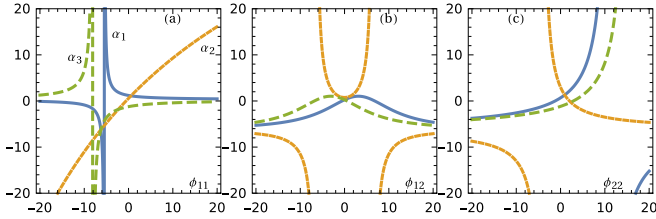
FIG. 2. Inverse solutions α_1 (solid line), α_2 (short dash), and α_3 (long dash) as functions of the various elements of the data matrix for $g = 0.1$. Left panel: ϕ_{11} is variable while $\phi_{12} \approx 2.534$ and $\phi_{22} \approx 0.504$. Center panel: ϕ_{12} is variable while $\phi_{11} \approx 1.465$ and $\phi_{22} \approx 0.504$. Right panel: ϕ_{22} is variable while $\phi_{11} \approx 1.465$ and $\phi_{12} \approx 2.534$. The triplet of values $(\phi_{11}, \phi_{12}, \phi_{22}) \approx (1.465, 2.534, 0.504)$ corresponds to $(\alpha_1, \alpha_2, \alpha_3) = (1, 2, -1)$.

surfaces on which the discontinuity occurs, the ISP is severely ill-posed. However, if the solution was unique in the linear regime, it remains unique for almost all values of the data matrix, except exactly at the surfaces of discontinuity where the inverse solution does not exist. In the simple case considered here, it is relatively easy to define the region around the origin of the three-dimensional space $(\phi_{11}, \phi_{12}, \phi_{22})$ in which the inverse solutions are continuous. In multidimensional problems, finding the discontinuities can become complicated. Yet, if the linearized ISP is well posed, a region of continuity of the nonlinear inverse solutions containing the origin always exists.

C. Discussion

The intermediate conclusion that we can draw is that accounting for multiple scattering does not necessarily make the ISP better posed and might not provide additional information about the target that is not available in the linear regime. However, if the linearized ISP is well posed and has a unique solution, the same remains true in the nonlinear case. The difficulty in this case is that the nonlinearity results in discontinuities in the dependence of the inverse solutions on the data, which, in the presence of experimental noise, can be detrimental.

The considered example also indicates that, in the case of nonuniqueness, the set of solutions is a curved manifold or a union of several such disjoint manifolds. The manifolds can be close to linear subspaces near the origin as is the case for the curve $g = 0.01$ in Fig. 1, which is almost a straight line near the origin but starts to curve as one moves further away. It can be pointed out that the curve $g = 0$, which is truly a straight line, is a mathematical abstraction; it does not represent a set of possible solutions to any physical inverse problem since all such problems have $g \neq 0$.

It remains for us to discuss why the measurement scheme based on the two vectors u and v resulted in a band-limited problem (Sec. III A) whereas the choice of u and w in the same context resulted in a well-posed problem (Sec. III A). This seems counterintuitive since all vectors in a Hilbert space are equivalent; one can be obtained from another by a simple rotation and dilation. The answer to the posed question is that what matters are entrywise (Hadamard) products of various pairs of the basis vectors. For example, if x = y ∘ z, then

$x_n = y_n z_n$. We can construct in this manner the following three vectors from u and v:

$$\mathtt{u} \circ \mathtt{u} = \begin{bmatrix} 1 \\ 1 \\ 1 \end{bmatrix}, \quad \mathtt{u} \circ \mathtt{v} = \begin{bmatrix} 1 \\ -2 \\ 1 \end{bmatrix}, \quad \mathtt{v} \circ \mathtt{v} = \begin{bmatrix} 1 \\ 4 \\ 1 \end{bmatrix}.$$

These vectors are linearly dependent. However, if we use u and w for the same purpose, we generate the following three vectors:

$$\mathtt{u} \circ \mathtt{u} = \begin{bmatrix} 1 \\ 1 \\ 1 \end{bmatrix}, \quad \mathtt{u} \circ \mathtt{w} = \begin{bmatrix} 1 \\ 0 \\ -1 \end{bmatrix}, \quad \mathtt{w} \circ \mathtt{w} = \begin{bmatrix} 1 \\ 0 \\ 1 \end{bmatrix}.$$

These vectors are in fact linearly independent.

IV. EXAMPLE WITH N DEGREES OF FREEDOM (INVERSE PROBLEM ON A FULLY CONNECTED GRAPH)

We now consider N particles characterized by possibly complex polarizabilities α_n and introduce the DFT of these variables (assuming for simplicity that N is odd) according to

$$\tilde{\alpha}_m = \sum_{n=1}^{N} \alpha_n e^{i\xi nm}, \tag{38a}$$

where

$$-M \leqslant m \leqslant M, \quad M = \frac{N-1}{2}, \quad \xi = \frac{2\pi}{N}. \tag{38b}$$

The inverse relation is

$$\alpha_n = \frac{1}{N} \sum_{m=-M}^{M} \tilde{\alpha}_m e^{-i\xi nm}. \tag{39}$$

The system under consideration can be visualized as a one-dimensional chain of particles in which the index n labels the coordinate. The setup of this section is directly relevant to the problem of inverse scattering. Moreover, the resolution limit can now be given a physically relevant definition.

In this section, similarly to Sec. III, we assume that all pairwise interactions in the system are given by the same parameter g so that $G_{nm} = g(1 - \delta_{nm})$. We can refer to this interaction as to *fully connecting* since it corresponds to the interactions of vertices in a fully-connected graph. Therefore, this section is a generalization of Sec. III to N degrees of freedom and also to more realistic measurement matrices, which now correspond to incoming and outgoing plane waves. The fully connecting interaction is not a physically realistic model but it will allow us to investigate the relevant mathematical features of the ISP analytically. In Sec. VI, we will consider a realistic interaction. To this end, we will have to resort to numerical simulations. However, we will perform a direct comparison of the realistic interaction to the fully-connecting interaction as well as to the tight-binding interaction and show that, at least from the point of view of nonlinear ISP, these cases are qualitatively similar. It is therefore useful to consider the fully connecting interaction to gain additional theoretical insight.

For the fully connecting interaction considered here, the T matrix of the system is given by a generalization of (20),

namely,

$$T_{nm} = \kappa_n \delta_{nm} + g \frac{\kappa_n \kappa_m}{1 - g\tilde{\kappa}_0} \ , \quad 1 \leqslant n, m \leqslant N. \qquad (40)$$

Here $\tilde{\kappa}_0 = \sum_{n=1}^{N} \kappa_n$ is the zeroth Fourier coefficient of κ_n.

Further, let the incident fields be given by a set of plane waves of the form $e^{i\xi ln}$, where $-L \leqslant l \leqslant L$, and let the detectors project the dipole moments of the particles onto the set of the same plane waves. Then the elements of the measurement matrices A and B are defined as follows:

$$A_{ln} = e^{-i\xi ln}, \quad B_{nl} = e^{i\xi nl}, \qquad (41a)$$

where

$$-L \leqslant l \leqslant L, \quad 1 \leqslant n \leqslant N. \qquad (41b)$$

This measurement scheme is characteristic of far-field excitation and detection.

Given the above definitions, equation (16) takes the form

$$\tilde{\kappa}_{l-j} + g \frac{\tilde{\kappa}_l \tilde{\kappa}_{-j}}{1 - g\tilde{\kappa}_0} = \phi_{jl}, \quad -L \leqslant j, l \leqslant L, \qquad (42)$$

where we have introduced the DFT of κ_n (denoted by $\tilde{\kappa}_m$) according to the convention (38a).

A. Linearized problem

In the limit $g \to 0$, we have $\kappa_n = \alpha_n$ and Eq. (42) is reduced to the following linear problem:

$$\tilde{\alpha}_{l-j} = \phi_{jl}, \quad -L \leqslant j, l \leqslant L. \qquad (43)$$

The physical admissibility condition for the Φ-matrix is in this case that it be banded so that $\phi_{jl} = f(l - j)$, where $f(\cdot)$ is any function. Assuming that Φ is physically admissible, (43) defines all Fourier coefficients $\tilde{\alpha}_m$ in the interval $-2L \leqslant m \leqslant 2L$. If $2L < M$, we say that the linearized problem is band-limited: one can recover only the Fourier coefficients $\tilde{\alpha}_m$ with the indexes m satisfying the above inequality. The high-frequency Fourier coefficients, that is, those with the indexes in the interval $2L < |m| \leqslant M$ are, in principle, unrecoverable from the data.

Note that the band limit is $2L$ rather than L. This is analogous to the radius of the Ewald sphere being twice the free-space wave number.

B. Full nonlinear problem

In the full nonlinear case, we must solve Eq. (42) for $\tilde{\kappa}_m$. If all $\tilde{\kappa}_n$ with $-M \leqslant m \leqslant M$ can be found from this equation (denote this result by $\tilde{\kappa}_n^{\text{inv}}$), we can use the inverse DFT to compute κ_n^{inv} for $1 \leqslant n \leqslant N$ and then find all α_n from $\alpha_n^{\text{inv}} = \kappa_n^{\text{inv}}/(1 - g\kappa_n^{\text{inv}})$. This is possible only if Φ is physically admissible, which we assume below.

However, (42) does not contain Fourier coefficients $\tilde{\kappa}_m$ with $|m| > 2L$ and therefore these coefficients can not be determined from the equation. For m within the band limit, we have the following solution:

$$\tilde{\kappa}_m^{\text{inv}} = \begin{cases} \frac{\phi_{0m}}{1 + g\phi_{00}}, & -L \leqslant m \leqslant L \\ \phi_{-L,m-L} - g\frac{\phi_{0L}\phi_{0,m-L}}{1 + g\phi_{00}}, & L < m \leqslant 2L \\ \phi_{L,m+L} - g\frac{\phi_{0,-L}\phi_{0,m+L}}{1 + g\phi_{00}}, & -2L \leqslant m < -L . \end{cases}$$

$$(44)$$

This is not a unique expression but, if Φ is physically admissible, then all such expressions are equivalent. For $|m| > 2L$, the solution can not be recovered in any way from the data.

We thus see that the nonlinear solution (44) is band-limited with respect to the Fourier coefficients $\tilde{\kappa}_m$. Indeed, all such coefficients with $|m| > 2L$ are unknown and can not be reconstructed in the measurement scheme considered here. But this does not mean that the inverse solution for α_n is also band limited. In fact, a set of α_n that is consistent with (44) but otherwise arbitrary is unlikely to be band limited.

The crucial point here is that the above observation does not mean that we have achieved super-resolution by solving a nonlinear ISP. Even though a typical set of α_n's that is consistent with (44) is not band-limited, there is no reason to believe that the high-frequency Fourier coefficients of this solution are correct. In fact, there is no reason to believe that *any* Fourier coefficients of this solution are correct. Indeed, there is no way to compute any of the unknowns α_n if we know only a limited subset of $\tilde{\kappa}_n$'s and do not know the rest. In any reconstruction method, we would be forced to make some *a priori* assumptions about these unknown quantities. In fact, all numerical solutions to ill-posed nonlinear ISPs involve such assumptions either explicitly or not. So, whereas in an ill-posed linearized ISP we know at least *some* Fourier coefficients of the unknown quantities α_n with certainty, in the nonlinear case *none* of the Fourier coefficients of α_n are known. Instead, the nonlinear equations provide some more general constraints, which are not easily amenable to Fourier analysis.

These theoretical considerations can be illustrated with the following numerical example. Consider N particles with some model polarizabilities α_n^{mod}. For simplicity, these quantities are taken to be real-valued in the simulations. Given the model for α_n's, we can compute the quantities κ_n^{mod} and then we can compute the forward DFT of κ_n^{mod} according to the convention (38a). This will produce a set of Fourier coefficients $\tilde{\kappa}_m^{\text{mod}}$ for $-M \leqslant m \leqslant M$. We then assume that the quantities $\tilde{\kappa}_m$ are known within the band limit, that is, $\tilde{\kappa}_m = \tilde{\kappa}_m^{\text{mod}}$ for $-2L \leqslant m \leqslant 2L$. The rest of the coefficients, that is, those with $2L < |m| \leqslant M$, are unknown from the data. In a practical reconstruction problem, we would be forced to make some *a priori* assumption about these coefficients. They can be set to any value without violating the governing nonlinear equations. The simplest choice is to set these quantities to zero. Then, given the complete set of Fourier coefficients $\tilde{\kappa}_m$ with $-M \leqslant m \leqslant M$ (some of which are "correct" and inferred from the data while the others are guessed), we can proceed with the algorithm outlined in the beginning of this subsection. That is, we apply the inverse DFT to compute κ_n^{inv} and then use the formula $\alpha_n^{\text{inv}} = \kappa_n^{\text{inv}}/(1 - g\kappa_n^{\text{inv}})$ to find the complete set of α_n^{inv}. Of course, the resultant α_n^{inv} will be different from α_n^{mod}.

In the simulation, we have taken $N = 1001$ so $M = (N - 1)/2 = 500$ and $L = 25$, and $M/2L = 10$. The model consists of several pulses of various width. The results are shown in Fig. 3. In the Fig. 3(a), we have taken $g = 0$ and the "reconstruction" performed by the algorithm described above simply yields the low-pass filtered version of α_n^{mod}. Since $M/2L = 10$, we expect that this reconstruction will resolve the features of about 10 units of length in width; oscillations or features
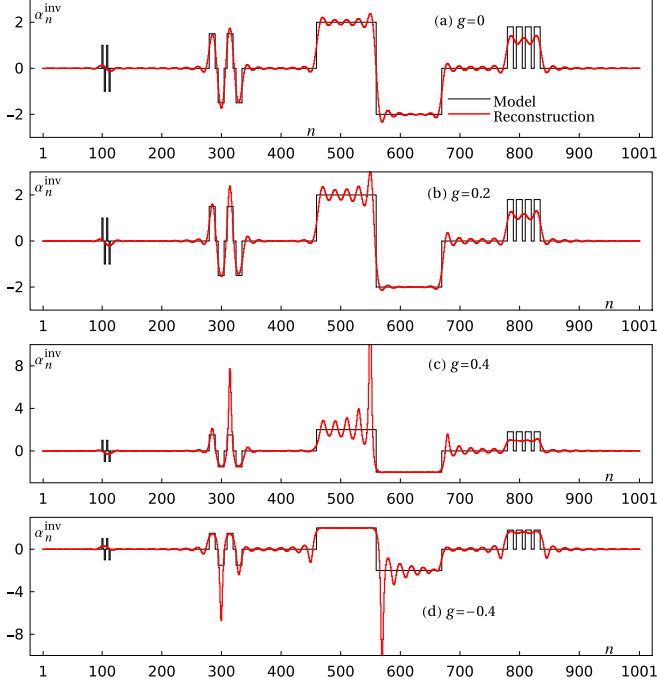
FIG. 3. Inverse solutions for $N = 1001$ and $L = 25$ (band limit of the linearized ISP is $2L = 50$) and various values of the interaction parameter g. The model polarizabilities α_n are purely real. However, nonlinear reconstructions are complex; only real parts are shown in the plots. (a) ($g = 0$) corresponds to the usual band-limited linearized reconstruction of α_n from ideal data. The plots in (c) and (d) extend beyond the figure frames and reach the values of ≈ 17 (c) and ≈ -17 (d).

that change on a smaller scale should not be resolvable. As can be seen from the Figure, this is, indeed, the case. Then, as the interaction strength g increases, the reconstructions acquire some sharp features due to the appearance of nonzero high-frequency Fourier coefficients of $\alpha_n^{\rm rec}$. But these Fourier coefficients are incorrect and the sharp features are in the wrong places; they do not help resolve the fine structure of the model at all. In fact, when $g = \pm 0.4$, all Fourier coefficients in the reconstruction are incorrect: even the integral (the sum of all $\alpha_n^{\rm rec}$'s) is predicted incorrectly. We note that the sharp features seen in the Panels (c) and (d) extend way beyond the figure frames and are truncated to make the graphical representation of the data manageable. Note that, for a real-valued model, the symmetry property $\tilde{\alpha}_{-m} = \tilde{\alpha}_m^*$ should theoretically hold. However, in the nonlinear reconstruction, this property is lost. Therefore, reconstructed values $\alpha_n^{\rm rec}$ are generally complex; only the real parts of $\alpha_n^{\rm rec}$ are shown in Fig. 3.

In Fig. 4, we show the power spectra, that is, the squared absolute values of the Fourier coefficients $|\tilde{\alpha}_m|^2$ for the model, the low-pass filtered model and the nonlinear reconstruction with $g = 0.4$. It can be seen that the nonlinear reconstruction is not band limited; however, its power spectrum is very different from the power spectrum of the model. Only for small indexes m is there some resemblance.

In Fig. 5, we show what would happen if, instead of setting the unknown coefficients $\tilde{\kappa}_m$ to zero, we assigned them some random values. Specifically, we have set the quantities $\tilde{\kappa}_m$ with

$2L < |m| \leqslant M$ to r_m, where r_m are pseudo-random numbers uniformly distributed in the interval $[-R, R]$. For the example shown in Fig. 5, we have taken $R = 100$. One can say that the linearized reconstruction is still recognizable while the nonlinear version is badly distorted. Note the different vertical scales in the Panels (a) and (c).

To illustrate the effects of noise, we have simulated reconstruction with noisy data. To this end, we have, first, used the model to generate the "ideal" data according to (42). Specifically, we have used the values $\alpha_n^{\rm mod}$ to compute $\kappa_n^{\rm mod} = \alpha_n^{\rm mod}/(1 + g\alpha_n^{\rm mod})$. Then the set of $\kappa_n^{\rm mod}$ were Fourier-transformed and substituted into the left-hand side of (42) to generate the forward data ϕ_{jl}. We then added to each element ϕ_{jl} a mathematically-independent complex quasi-random number according to the prescription

$$\phi_{jl} \longrightarrow \phi_{jl} + R\sqrt{\langle |\tilde{\kappa}_{j-l}^{\rm mod}|^2 \rangle} Z , \qquad (45)$$

where R is the noise level and Z is a complex random variable with the following statistical properties. The absolute value $|Z|$ is distributed according to one-half of the

FIG. 4. Power spectra of the model (a), of the low-pass filtered model (b) and of the nonlinear reconstruction with $g = 0.4$ (c) for the same numerical example and parameters as in Fig. 3.
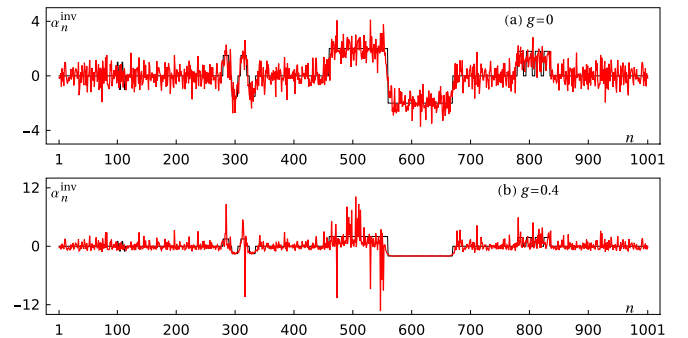
FIG. 5. Same reconstructions as in Figs. 3(a) and 3(c), but the unknown coefficients $\tilde{\kappa}_m$ were set to pseudorandom numbers r_m uniformly distributed in $[-R, R]$, where $R = 100$. The data of Fig. 3 are obtained by setting $R = 0$.
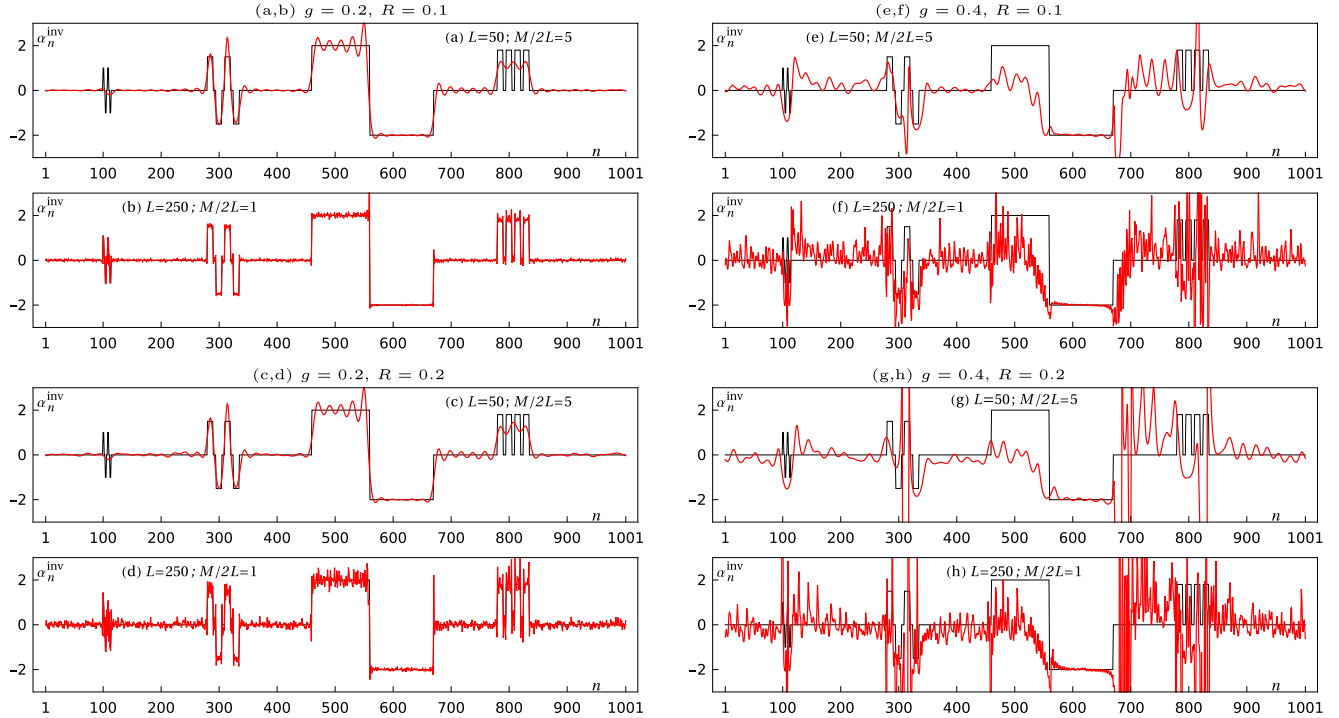
FIG. 6. Nonlinear reconstructions of the same model as in Fig. 3 for $g = 0.2$ (a)–(d) and $g = 0.4$ (e)–(h) and different levels of noise in the data as quantified by the parameter R according to (45). In (a), (b), (e), (f), $R = 0.1$ and in (c), (d), (g), (h) $R = 0.1$. Reconstructions are performed for different bandwidths of the measurements, as quantified by the ratio $M/2L$. Two cases are considered: band-limited measurements with $M/2L = 10$ (a), (c), (e), (g) and complete (not band-limited) measurements with $M/2L = 1$ (b), (d), (f), (h).

normal distribution with the unit variance, i.e., $P(|Z|) = \sqrt{2/\pi} \exp(-|Z|^2/2)$, and the complex phase of Z is uniformly distributed between 0 and 2π. Note that the square-root factor in (45) is the root mean square value of the elements of the data matrix in the linear regime (i.e., when $g = 0$). The same noise up to the multiplicative factor R, which was varied, was added to the ideal data, independently of g or the bandwidth that was used in the reconstruction. Finally, using the noisy data defined by (45), we computed the nonlinear inverse according to (44).

Results of reconstructions with noisy data are shown in Fig. 6. It can be seen that, in the case of weak nonlinearity ($g = 0.2$), the reconstructions are relatively stable. This is expected since the reconstruction in this case is "almost" an inverse Fourier transform. As the Fourier transform operator has a flat spectrum of singular values, its inversion is numerically stable. Moreover, it can be seen that, in the case of a band-limited reconstruction ($M/2L = 10$), the noise is largely suppressed. This is similar to suppression of the uncorrelated white noise by low-pass spectral filtering. However, when nonlinearity is increased ($g = 0.4$), reconstructions become much more sensitive to noise. Indeed, the nonlinear inverse solutions are discontinuous. As g is increased, the data approach the surfaces of discontinuity of the inverse solution (this is illustrated, for example, in Fig. 2 above). Since the inverse solution is highly nonlinear close to the surfaces of discontinuity, it is also numerically unstable: small errors in the data tend to be amplified. This is easy to understand by considering the function $1/(x + r)$ where r is noise. When x is far from zero (much further than $\sqrt{\langle r^2 \rangle}$), the above function is numerically stable. However, this is not so when $|x| \lesssim \sqrt{\langle r^2 \rangle}$.

So far we did not consider very strong nonlinearities. If we take, say, $g = 5$ and keep the band limit at the level $M/2L = 10$, a sensible reconstruction is not possible even with ideal data. But as L increases, progressively better reconstructions are obtained. If the linearized ISP is well posed (when $2L = M$), we know that the full nonlinear ISP also has a unique solution. This behavior is illustrated in Fig. 7. Here we increase L gradually from 50 to 240. In the latter case, the ratio $2L/M$ is very close to but still not quite unity. It can be seen that all but the finest features are well resolved and the nonlinearity does not play a very detrimental role for $L = 240$. If we take $L = 250$ so $2L = M$, the resulting reconstruction is perfect in the absence of data noise (data not shown). However, the reconstruction for $L = 50$ is hardly meaningful. Compare this to Fig. 1(a), which shows the low-pass filtered version of the model. The latter is quite useful. In comparison, the reconstruction in the strong nonlinearity regime with the twice-as-large band limit [Fig. 7(b)] is not useful at all. It should also be noted that reconstructions at $g = 5$ are extremely sensitive to noise. If we use the same noise that was used in Fig. 6, all reconstructions already become very noisy when $R = 0.01$ and are completely destroyed at $R = 0.1$.

V. TANGENT VECTORS AND SPACES

So far, we have relied on exactly solvable toy problems. In more realistic cases, neither the forward nor the inverse problem can be solved analytically. However, there exists a powerful numerical approach that allows one to investigate the possibility of super-resolution in a generic setting. The
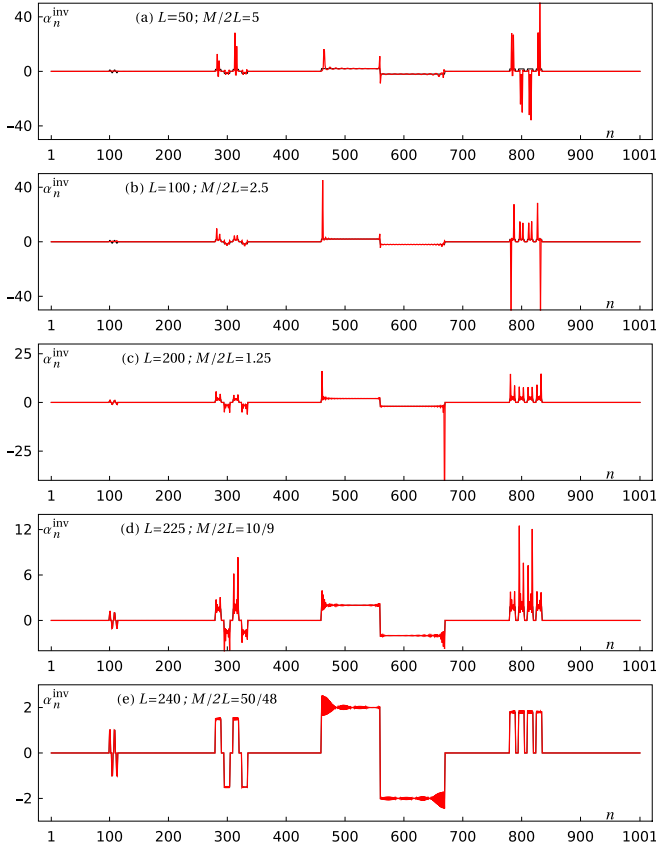
FIG. 7. Nonlinear reconstructions of the same model as in Fig. 3 for $g = 5$ and different bandwidths of the measurements, as quantified by the ratio $M/2L$. For complete (not band-limited) measurements, we have $M/2L = 1$; otherwise, $M/2L > 1$.

method is based on examining the tangent spaces at various points of the manifold of solutions to the nonlinear ISP. This approach is explained below.

A. Distorted Born approximation

Consider a nonlinear ISP as defined by Eq. (16). Let D be some generic potential. We are interested in a small vicinity of D. Let

$$U = D + V, \tag{46}$$

where V is in some sense small. First, we have nonvanishing order in V:

$$T[U] = T[D + V] \approx T[D] + S[D] \, V \, S^T[D], \tag{47}$$

where $T[\cdot]$ is given by (14) and $S[\cdot]$ is defined by

$$S[X] = (I - XG)^{-1}, \quad S^T[X] = (I - GX)^{-1}. \tag{48}$$

It follows from the symmetry of all matrices involved that the two expressions given above are transposes of each other. Note the relations

$$T[X] = S[X] \, X = X \, S^T[X]. \tag{49}$$

Thus, in the vicinity of D, Eq. (16) takes the following form:

$$(AS[D]) \, V \, (S^T[D]B) = \Phi - A \, T[D] \, B \equiv \Psi[D]. \tag{50}$$

Assuming that Φ is measured and D is known, (50) is a linear equation with respect to V. The approximation involved in deriving (50) is known as the *distorted Born approximation*. In fact, there is no big conceptual difference between the ordinary Born and the distorted Born approximations. The former is just a special case of the latter obtained when $D = 0$. Equation (50) provides a linearization of (16) near some generic potential D, which is not necessarily zero.

B. Examination of uniqueness

It can be easily seen that (50) is the equation that one would use in order to find small deviations of the total potential U from the known background D. Let a data matrix Φ be measured in an experiment or simulated by solving a forward problem. We wish to find the potential U that corresponds to this Φ. If Φ is not small, we have no reason to suspect that the corresponding U is small. So we cannot linearize the ISP in U. Now assume that we have some additional information about U, namely, that it can be written in the form (46) where D is known and not necessarily small whereas V is small but otherwise unknown. Since D is known, we can also compute $S[D]$, $T[D]$, and then $\Psi[D]$ by using (48)–(50). The problem is now to find V by solving the linear equation (50). But is the solution unique?

Let us assume that this solution is indeed unique and denote it by V^{inv}. Then the nonlinear ISP has the solution $U^{inv} \approx D + V^{inv}$ and there are no other solutions in the vicinity of D [52]. There might be other solutions elsewhere, so we have not proved global uniqueness. However, there exists a finite radius $R > 0$ such that there is only one solution in the N-dimensional ball of radius R centered at D; the map $U \rightarrow \Psi$ is locally invertible in the vicinity of D. This is guaranteed by the inverse function theorem; existence of the unique inverse solution to (50), V^{inv}, is equivalent to the condition that the Jacobian derivative of the functional $F[U] \equiv AT[U]B$ that is defined by the left-hand side of (16) is nonzero at $U = D$.

On the other hand, if (50) does not have a unique solution, then we have strong reasons to suspect that the solution to the original nonlinear ISP (16) is also nonunique. We do not know this for sure due to the possible exception noted below in Sec. V C. However, the following statement is true. Let D itself be a particular solution to (16) selected from the set of all possible solutions (this implies $\Psi[D] = 0$). Let also R_n ($n = 1, 2, \ldots$) be diagonal matrices that satisfy

$$(AS[D]) \, R_n \, (S^T[D]B) = 0. \tag{51}$$

Then the potential $U_n(\epsilon) = D + \epsilon R_n$ satisfies the nonlinear ISP (16) with the precision of at least $O(\epsilon^2)$. To see that this is indeed the case, we linearize (16) near D, substitute $V = \epsilon R_n$ into the resulting linearized equation (50) and see that the equation is satisfied by this substitution. So the error of the equation is zero to first order in ϵ. The first nonvanishing correction to this result is obviously of the order $O(\epsilon^2)$ or higher. Under the "normal" circumstances (discussed below in Sec. V C), this means that the set of solutions to (16) forms a manifold of which D is a particular point and that one can define one or more orthogonal tangent directions to this manifold at D. These directions span the tangent space. We will say that the

number $r(\mathsf{D})$ of linearly independent matrices R_n that satisfy (51) is the dimensionality of this tangent space at the point D.

We can therefore investigate the degree of ill-posedness of a nonlinear ISP by analyzing the linear operator in Eq. (50). If the corresponding linearized ISP is band limited, we know for sure that the tangent space at $\mathsf{D} = 0$ is not empty so that $r(0) > 0$. For one-dimensional targets characterized by the coefficients α_n, $r(0)$ is equal to the number of Fourier coefficients $\tilde{\alpha}_m$ that lie outside of the band limit and, consequently, are not coupled to the data. If $\mathsf{D} \neq 0$, we no longer have this simple interpretation of the tangent space. However, we can attempt to answer the following question numerically. Assume that $r(0) > 0$. Is it possible that, for some $\mathsf{D} \neq 0$, $r(\mathsf{D}) < r(0)$ and, moreover, is it possible that $r(\mathsf{D}) = 0$? Any of these outcomes entails achieving some super-resolution, although to varying degrees. In the best possible case, $r(\mathsf{D}) = 0$ implies that the potential D can be recovered uniquely without any loss of resolution by solving the nonlinear ISP, assuming that the data are noiseless.

C. A word of caution

Above, we have, essentially, relied the inverse function theorem. However, this theorem provides only a sufficient, and not a necessary condition for a map to be locally invertible. The counter-examples in which the conditions of the theorem are not met but a function is invertible usually involve surfaces or curves that touch at a point. Perturbation theory (in the interaction) is in such cases singular and should be approached with caution. Here we present a simple albeit an abstract example, which illustrates the same mathematical point. A more relevant but also much more complicated example is analyzed in Appendix A, but the inverse solution for that model is very complicated.

Consider two equations with two unknowns,

$$y - g^2 x^2 = \phi_1, \quad y = \phi_2, \tag{52}$$

which describe a parabola and a straight line. If $\phi_1 = \phi_2 = b$, the parabola touches the straight line at the point $(0, b)$. Thus, if the data matrix is given by $\Phi = (b, b)$, the set (52) has the unique solution $(0, b)$. The conditions of the inverse function theorem are however not satisfied at this point. Indeed, the Jacobian derivative of the forward functional is given by

$$J = \det \begin{bmatrix} -2g^2 x & 1 \\ 0 & 1 \end{bmatrix} = -2g^2 x. \tag{53}$$

At the point $(0, b)$, the Jacobian is zero.

Another feature of (52) is that the perturbation expansion of the inverse solution is singular when $g \to 0$. Indeed, we have

$$x^{\mathrm{inv}} = \pm \frac{1}{g} \sqrt{\phi_2 - \phi_1}, \quad y^{\mathrm{inv}} = \phi_2. \tag{54}$$

This solution is not defined at $g = 0$ (a limit $g \to 0$ may exist if the data are ideal). However, the conditions of the inverse function theorem are satisfied in the vicinity of any point $(x^{\mathrm{inv}}, y^{\mathrm{inv}})$ given by (54) as long as $x^{\mathrm{inv}} \neq 0$ or in the vicinity of any point (ϕ_1, ϕ_2) in the data space as long as $\phi_1 \neq \phi_2$. Under these conditions, the two curves defined by (52) intersect rather than touch. The map (52) is in this

case locally (but not globally) invertible and the analysis of Sec. V B fully applies.

The questions we wish to address now are: (i) Is (52) an example of super-resolution due to nonlinearity? (ii) Do equations of this kind arise in practical ISPs? (iii) If they do, can we analyze them numerically as suggested in Sec. V B?

The answer to question (i) is positive: Definitely, (52) has a unique solution (modulo the sign of x^{inv}) only if $g \neq 0$. So, the nonlinearity forces uniqueness in this example.

The answer to question (ii) is more nuanced. Equations of the form similar to (52) can arise in practical problems and the numerical examples shown below indicate that they do arise. However, the simulations also indicate that this effect is insignificant because, in systems with many degrees of freedom, the number of such equations is relatively small. Consequently, the dimensionality of the manifold of solutions is not decreased substantially due to such occurrences.

Question (iii) can be answered as follows. If super-resolution exists, the numerical technique proposed in this paper should discover this by considering $r(\mathsf{D})$ at several different points D. The test can fail at some particular point D_0. That is, the tangent space dimensionality can be larger at D_0 than the actual dimensionality of the manifold of solutions. In the extreme case, the tangent space may appear to be non-empty whereas the nonlinear equations have in fact a locally unique inverse. However, occurrences of this sort are likely to be rare exceptions; they require that many multi-dimensional surfaces described by the forward nonlinear equations touch at one point. By trying different D's, i.e., randomly-generated, one is certain to find that the tangent space is almost always empty *if* the ISP, indeed, has a unique solution. So, the numerical analysis proposed in this paper is reliable if used properly.

Finally, in the above discussion, we interpret "touching" of two surfaces at a point in a somewhat broader sense than usual and include the possibility of an intersection with a saddle point, as in the case of two lines $y = x^3$ and $y = 0$.

VI. EXAMPLE WITH A REALISTIC INTERACTION (SCALAR WAVE INVERSE DIFFRACTION)

In this section, we introduce an interaction that is relevant to the scalar wave tomography, i.e., in the ultrasound or seismic imaging. Although we still consider one-dimensional targets, the interaction is characteristic of three-dimensional space. We can say that the target is simply a special case of a more general three-dimensional object. Neither the forward nor the inverse problem are solvable analytically for the interaction considered in this section. We will therefore resort to numerical simulations. Chains of particles (or voxels) of $N = 51^2 = 2601$ independent degrees of freedom will be used in the numerical examples. We will apply the ideas of Sec. V and investigate the dimensionality of the tangent space $r(\mathsf{D})$.

A. Model setup

The forthcoming numerical examples involve the realistic interaction of the form

$$G_{nm} = g(1 - \delta_{nm}) \frac{e^{ik|\mathbf{r}_n - \mathbf{r}_m|}}{|\mathbf{r}_n - \mathbf{r}_m|/h}, \tag{55}$$

where g is a dimensionless parameter quantifying the strength of interaction, $\mathbf{r}_n$ are the positions of the particles, $k = \omega/c = 2\pi/\lambda$ is the free-space wave number, and h is the interparticle spacing (or the voxel size). The particles are arranged on a linear chain so $x_n = y_n = 0$ and $z_n = (n-1)h$, $n = 1, 2, \ldots, N$.

We have formulated the problem so that both the interaction matrix and the potential are dimensionless. We will use some model potentials for D in which the diagonal elements are of the order of unity and linearize the inverse problem near those points. The linearization will involve computing the matrices T[D] and S[D] nonperturbatively, i.e., by matrix inversion according to (14) and (48). These formulas depend on the interaction matrix G and the latter is proportional to the dimensionless parameter g. We will vary g to control the strength of nonlinearity in the ISP.

In the examples shown below, we compare two cases. In the the first case, we take $L = 51$ and $N = L^2 = 2601$. Correspondingly, $M = 1300$ and $M/2L \approx 13$. For this choice of parameters, the linearized ISP is severely band limited; only about $1/13$ of all DFT coefficients of the target are known from the data. In the second case, N and M are the same but $L = 650$, so $M = 2L$ and $N = 4L + 1$. In this case, the linearized ISP is well posed and not band limited.

In all cases, we have defined the wave number in (55) as $k = 2\pi L/Nh$, so it coincides with the largest spatial frequency that is present in A and B. In other words, we assume that the incident and the outgoing plane waves have a fixed wave number but can make different angles with the chain including the zero angle. Consequently, the measurement matrices are

$$A_{ln} = e^{-i(l/L)kz_n}, \quad B_{nl} = e^{i(l/L)kz_n}, \tag{56}$$

where $-L \leqslant l \leqslant L$ and $1 \leqslant n \leqslant N$. Here $(l/L)k$ is the projection of a plane-wave wave vector onto the chain. We can also write $l/L = \cos\theta$, where θ is the angle between the positive direction of the Z axis and the wave vector of an incident or an outgoing plane wave.

B. Linearized reconstructions

Let us first linearize (16) near D = 0. In the considered setting, a linearized reconstruction, that is, a solution to (18) with some known data matrix Φ, can be achieved by either low-pass filtered inverse DFT (for $L = 51$) or by the exact inverse DFT (for $L = 650$). However, we have used a more general and, as one can argue, a better [53] approach, and computed the inverse solution to (18) by the method described in Refs. [54,55]. Namely, it can be shown that the Tikhonov-regularized pseudoinverse solution to (18) can be obtained as the solution to the system of equations

$$(W[0] + \epsilon^2 w_{\max} I)\alpha = b, \tag{57}$$

where

$$W_{nm}[0] = (A^*A)_{nm}(BB^*)_{mn}, \tag{58}$$

ϵ is the regularization parameter, $w_{\max}$ is the maximum eigenvalue of W[0] (introduced in the formula for convenience), and
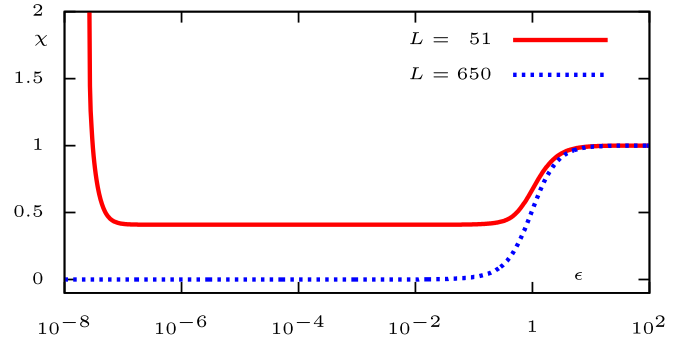
FIG. 8. Error χ (60) as a function of ϵ for the linearized inverse crime reconstruction obtained by solving (57) numerically. The target model 1 used to generate data for these reconstructions is illustrated in the subsequent figures.

the vectors α and b are defined by

$$\alpha = \begin{bmatrix} \alpha_1 \\ \alpha_2 \\ \cdots \\ \alpha_N \end{bmatrix}, \quad b = \begin{bmatrix} (A^*\Phi B^*)_{11} \\ (A^*\Phi B^*)_{22} \\ \cdots \\ (A^*\Phi B^*)_{NN} \end{bmatrix}, \tag{59}$$

Note that α consists of the diagonal elements of V. The matrix W[0] is square, Hermitian (self-adjoint) and non-negative definite so that (57) is well-posed. The argument "0" is used to indicate that W[0] is defined for D = 0; a more general matrix W[D] will be defined below for nonzero D.

As the first example, we have generated the data matrix Φ by substituting the model potential D = diag($\alpha_1^{\mathrm{mod}}, \ldots, \alpha_N^{\mathrm{mod}}$) in place of V in (18) and evaluating the left-hand side. We then pretended that Φ is known while V is not and sought to reconstruct the latter from the former. This procedure is known as "inverse crime". In Fig. 8, we show the error of such an inverse crime reconstruction, χ, as a function of ϵ for the parameters defined above and for the model D that is illustrated in the subsequent figures and referred to as model 1 (we have also used for comparison an alternative homogeneous model D = I, which we refer to as model 2). The error is defined as

$$\chi^2 = \frac{\sum_n |\alpha_n^{\mathrm{inv}} - \alpha_n^{\mathrm{mod}}|^2}{\sum_n |\alpha_n^{\mathrm{mod}}|^2}. \tag{60}$$

For $L = 51$, the error does not approach zero and is not particularly small. This is so because the linearized problem in this case is band limited. The minimum-L_2 norm solution that is found by solving (57) is not expected to reproduce the model precisely. However, the error is flat in a wide interval of ϵ. This is a characteristic feature of the low-pass filtered inverse DFT: the spectrum of W has a wide gap. We further note that, for $\epsilon \lesssim 10^{-7}$, numerical instabilities set in while, for $\epsilon \gtrsim 1$, the regularization is too crude. Indeed, we have $\alpha_n^{\mathrm{inv}} \to 0$ when $\epsilon \to \infty$; the corresponding error χ approaches unity in that limit, as follows from (60). In the case $L = 650$, the error approaches zero for sufficiently small ϵ and there are no numerical instabilities. Indeed, the matrix W[(0)] is in this case invertible and has no numerically small eigenvalues. The solution can be found by setting $\epsilon = 0$ in (57) and computing the ordinary matrix inverse.
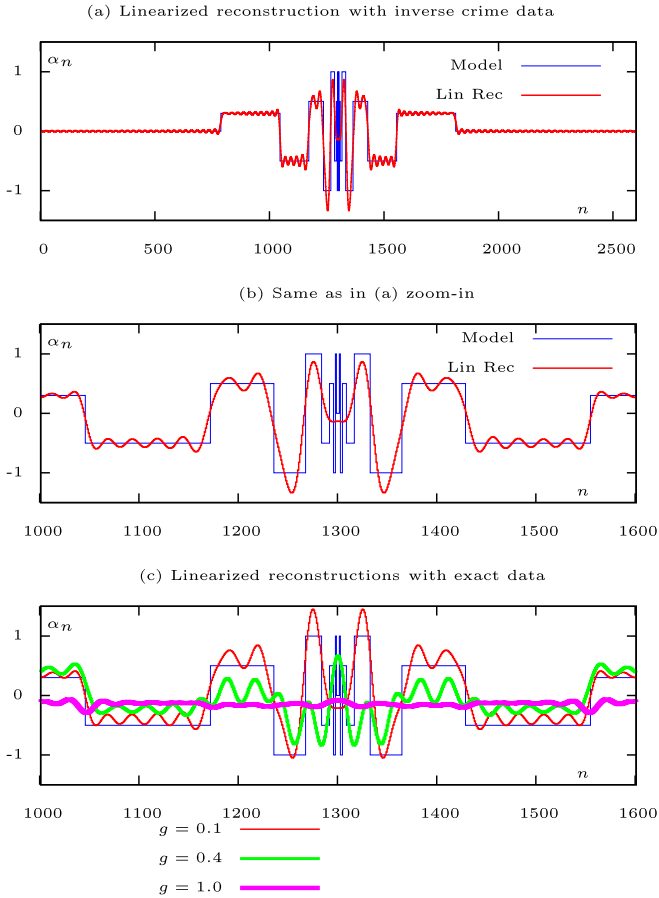
FIG. 9. Linearized reconstructions for $L = 51$ and inverse crime data generated from (18) (a) (b) and for the data obtained from the nonlinear Eq. (16) and $\mathtt{G}$ defined in (55) and various values of g, as labeled (c). In all cases, the same target $\mathtt{D}$ was used (a set of rectangular pulses shown the thin blue line in the plots). We refer to this target as model 1. Equation (57) was used for the reconstructions with $\epsilon = 10^{-3}$. The matrix $\mathtt{W}$ (58) was diagonalized numerically. The line keys correspond to (c): Thin (red) line represents the case $g = 0.1$, medium (green) line represents $g = 0.4$ and thick (purple) line represents $g = 1.0$.

Linearized reconstructions with the inverse crime data generated by using model 1 as the target are shown in Figs. 9(a) and 9(b) for $L = 51$ and in Figs. 10(a) and 10(b) for $L = 650$. Model 1 is shown in all plots as a thin blue line and consists of rectangular pulses of different widths. In both cases, we used $\epsilon = 10^{-3}$ for regularization; this value is well inside the gap of the spectrum of $\mathtt{W}[0]$. It can be seen that, in the case $L = 51$, the reconstruction is indeed a low-pass filtered version of the model. The pulses whose widths are of the order of 100 lattice units or larger are reconstructed more or less correctly, but the finer features are unresolved. In particular, the narrow pulses in the center of the target are completely lost. In contrast, the inverse crime reconstructions for $L = 650$ are perfect, just as expected.

In Figs. 9(c) and 10(c), we show for comparison the linearized reconstructions for which the data matrix Φ was computed from the "exact" nonlinear equation (16). The reconstructions were still performed assuming that the
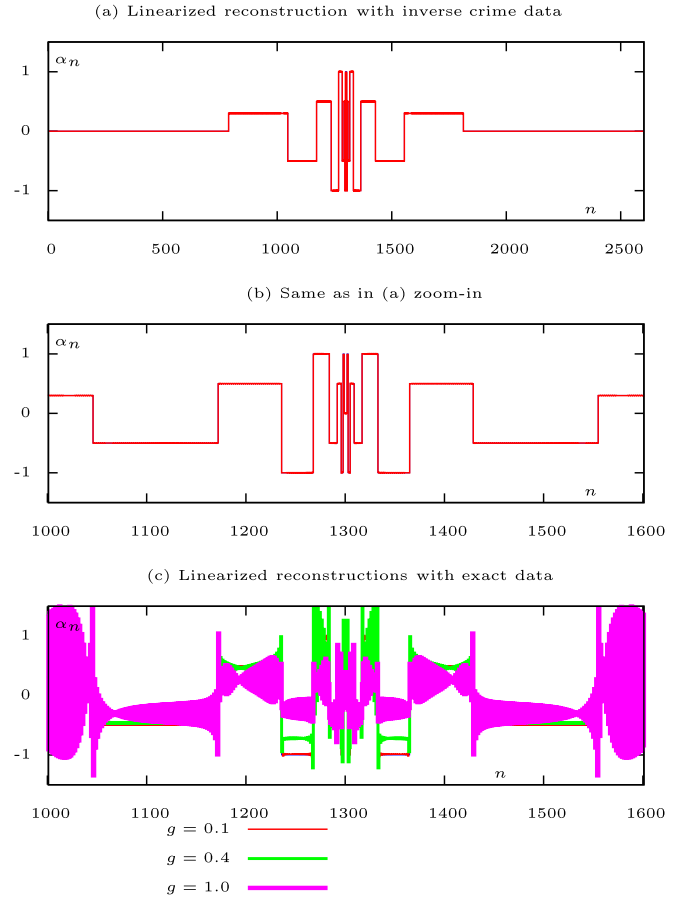
FIG. 10. Same as in Fig. 9 but for $L = 650$. The line representing the model is obscured in this figure but can be seen clearly in Fig. 9. The line keys correspond to (c): Thin (red) line represents the case $g = 0.1$, medium (green) line represents $g = 0.4$ and thick (purple) line represents $g = 1.0$.

linearization (18) is accurate and then using (57) for numerical inversion. Therefore, the reconstructions shown in Figs. 9(c) and 10(c) do not involve inverse crime. At the relatively small value $g = 0.1$, the effects of nonlinearity are negligible for both $L = 51$ and $L = 650$; the reconstructions are almost the same as the inverse crime linearized reconstructions. But at $g = 0.4$, the nonlinearity sets in and at $g = 1.0$ linearized reconstructions are no longer useful. The distortions are, however, quite different in the cases $L = 51$ and $L = 650$. In any event, we can conclude that the ISP is essentially nonlinear at $g = 0.4$ and severely nonlinear at $g = 1.0$.

C. Eigenvalues of $\mathtt{W}$ and dimensionality of the tangent space

The next question we address is whether the tangent space dimensionality near $\mathtt{D} \neq 0$ is different from that near $\mathtt{D} = 0$. To this end, we consider the distorted Born approximation (50) and view it as a linear equation with respect to $\mathtt{V}$. In complete analogy to (58), we define the matrix $\mathtt{W}[\mathtt{D}]$ for the distorted Born approximation as

$$W_{nm}[\mathtt{D}]$$
$$= ((A S[\mathtt{D}])^* (A S[\mathtt{D}]))_{nm} ((S^{\mathtt{T}}[\mathtt{D}]B)(S^{\mathtt{T}}[\mathtt{D}]B)^*)_{mn}, \quad (61)$$
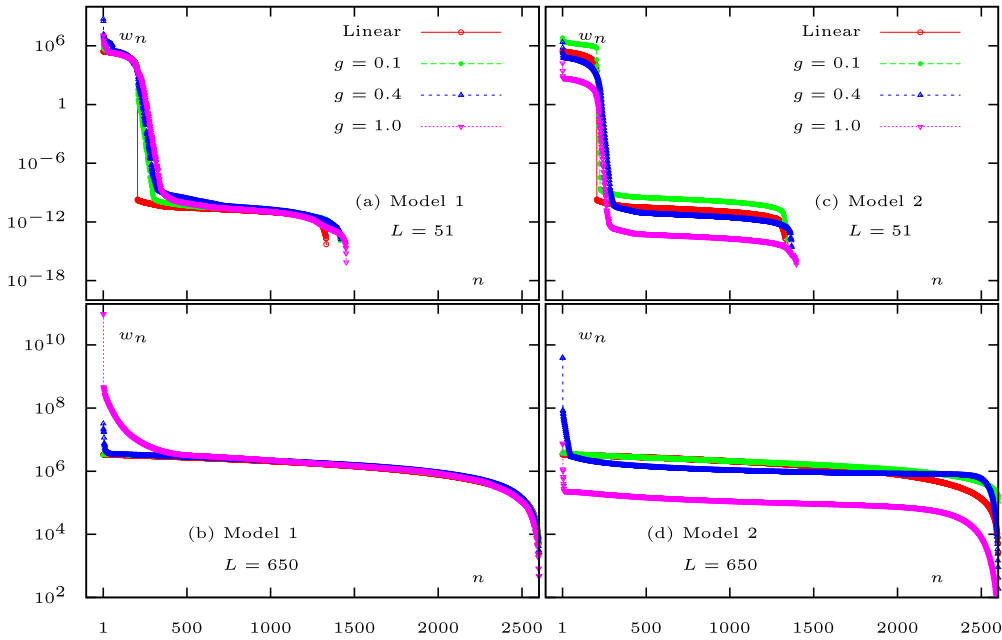
FIG. 11. Eigenvalues of $\mathtt{W[D]}$, $w_n[\mathtt{D}]$, for $L = 51$ (a), (c) and $L = \frac{51^2 - 1}{4} = 650$ (b), (d). $\mathtt{D}$ is given by model 1 (a), (b) or model 2 (c), (d), and different interaction strengths g are used as labeled. In model 2, $\mathtt{D} = \mathtt{I}$. In (a) and (c), eigenvalues with indexes that are greater than ~ 1500 are not numerically distinguishable from zero and therefore cannot be displayed using the vertical logarithmic scale.

where $\mathtt{S[D]}$ is defined by (48). If we evaluate $\mathtt{S[D]}$ at $\mathtt{D} = 0$ and substitute the result into (61), we would obtain the same matrix $\mathtt{W[0]}$ that was defined in (58). The same result can be obtained by formally setting $g = 0$ since, in this case, $\mathtt{S[D]} = \mathtt{I}$ irrespectively of $\mathtt{D}$. In what follows, we evaluate $\mathtt{S[D]}$ for two different models $\mathtt{D}$ and use different values of g to tune the degree of nonlinearity. The dimensionality of the tangent space $r(\mathtt{D})$ is equal to the number of zero eigenvalues of $\mathtt{W[D]}$. Of course, in numerical simulations, eigenvalues are never exactly zero. We will have therefore an additional task in front of us to determine which eigenvalues are significant (that is, essentially, nonzero) and which are insignificant. Only the latter contribute to the dimensionality of the tangent space. Although the choice is often easy, there exist borderline cases when it is not.

In Fig. 11, we display the eigenvalues of $\mathtt{W[D]}$ for different L, g and $\mathtt{D}$. Model 1 for $\mathtt{D}$ [Figs. 11(a) and 11(b)] is the same as the one used in Figs. 9 and 10. In Figs. 11(c) and 11(d), we show for comparison the results for the homogeneous model $\mathtt{D} = \mathtt{I}$ (Model 2).

Consider first the results for model 1 and $L = 51$ [Fig. 11(a)]. It can be seen that there exists a set of relatively large eigenvalues, which we will call significant, and then an abrupt jump of roughly 15 orders of magnitude. We will refer to the eigenvalues at the floor of this jump as insignificant. In the case $g = 0$, the jump is perfectly sharp. Theoretically, we can predict that, at $L = 51$, $\mathtt{W[0]}$ has exactly $4L + 1 = 205$ nonzero eigenvalues and the rest are zero. This is fully consistent with the numerical results. The small eigenvalues below the gap in the $g = 0$ data set are finite only due to the limited numerical precision of the computer. When $g > 0$, the above analysis does not apply since $\mathtt{W[D]}$ is no longer related in this case to a band-limited DFT. However, the numerical data indicate that the transition from significant to insignificant

eigenvalues still occurs, although it is not as sharp as in the case $g = 0$. The eigenvalues in the transition region will be discussed below separately.

We now discuss the data sets shown in Fig. 11(a) in more detail. First, we note that the significant eigenvalues are not constant but decrease with the index. This may seem to be counterintuitive since the nonzero singular values of the DFT operator are constant. It is, however, easy to understand this behavior in the case $g = 0$. In this case, the inverse problem of finding $\mathtt{V}$ from the data consists of inverting the linear equations in (18). This set contains redundant equations. For example, it contains $2L + 1$ equations of the form

$$\alpha_1 + \alpha_2 + \ldots + \alpha_N = \Phi_{l,-l}, \quad -L \leqslant l \leqslant L. \quad (62)$$

Note that $\alpha_1 + \alpha_2 + \ldots + \alpha_N = \tilde{\alpha}_0$ is the zeroth Fourier coefficient of α. We say that the equation for $\tilde{\alpha}_0$ in (18) has the statistical weight $2L + 1$. More generally, the equations for the Fourier coefficients $\tilde{\alpha}_m$ have the statistical weights that decrease linearly with $|m|$. The equations for $\tilde{\alpha}_{\pm 2L}$ have the statistical weights of 1. Equations for the higher coefficients have statistical weight 0, which means that these coefficients simply do not enter the equations. The spectrum of $\mathtt{W[0]}$ is defined by the above statistical weights. The linear dependence of the significant eigenvalues on the index for the $g = 0$ data set would be clearly visible in the plots if we used linear scale on both axes.

When $g > 0$, the perturbation $\mathtt{V}$ is coupled to the data by (50) rather than by (18). In this case, we can no longer assign statistical weights to the Fourier coefficients so easily; instead, all the Fourier coefficients of the diagonal elements of $\mathtt{V}$ are coupled to each other by (50). Still, the significant eigenvalues do not need to be constant. Moreover, in the cases $g = 0.4$ and $g = 1.0$, there appear some relatively large eigenvalues. This is due to the resonance phenomena. The matrix $\mathtt{S[D]}$ in (50)
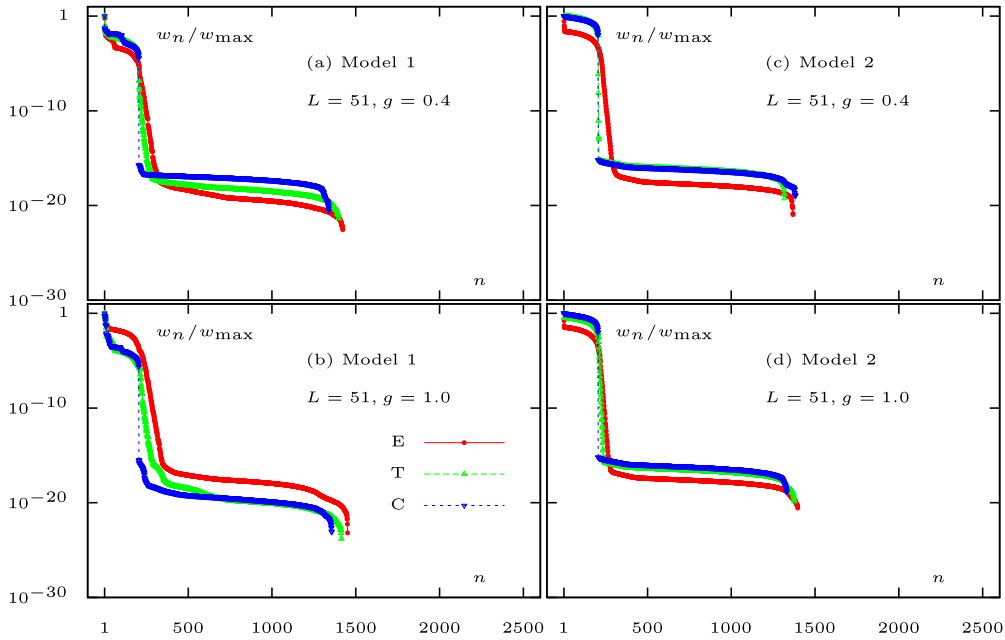
FIG. 12. Eigenvalues of W[D], w_n[D], normalized to the maximum eigenvalue for each spectrum. Results are compared for the same two models for D as in Fig. 11 and three different interactions G: exponential interaction (55) (E), the tight-binding interaction $G_{nm} = g(1 + 0.1i)(\delta_{n,m-1} + \delta_{n,m+1})$ (T), and the fully connecting interaction $G_{nm} = g(1 + 0.1i)(1 - \delta_{nm})$ (C). Parameters L and g as labeled.

is singular when one of the eigenvalues of GD is equal to 1. If GD is close to one of such singularities, the resultant matrix W[D] has one or several very large eigenvalues. Put simply, in this case, the scattered field becomes very sensitive to small changes in V (recall that the total potential is U = D + V where D is fixed) *in some directions* because the system goes in or out of resonance due to such changes.

Next, we discuss the transition from significant to insignificant eigenvalues. As can be seen in Fig. 11(a), a finite transition region exists when $g > 0$. The situation is somewhat similar to a band-limited but irregular Fourier transform. The spectra of singular values for such transforms also display a quasi-smooth transition, in contrast to the regular band-limited DFT whose spectrum has a perfectly sharp jump. However, the typical transition in an irregular band-limited Fourier transform is even sharper than what is displayed in Fig. 11(a). For example, a band-limited Fourier transform with the same parameters as those used in Fig. 11(a) and N Fourier wave numbers q_m randomly sampled between the bounds $-2(2\pi/N)L$ and $2(2\pi/N)L$ has the transition for the eigenvalue indexes, roughly, from $n = 4L + 1 = 205$ to $n \approx 250$ (data not shown). In contrast, the transition occurs between $n \approx 205$ and $n \approx 350$ in Fig. 11(a) (for $g = 1.0$).

While the effect of irregular sampling can play some role, we conclude that the nonlinear ISP in the vicinity of D given by model 1 is, indeed, better posed, albeit very slightly, than in the vicinity of D = 0. This can occur due to some additional statistically significant equations that can appear when $g \neq 0$, similarly to what is described analytically in Appendix A 2. Linearization of these equations near D gives rise to the transitional eigenvalues. We note, however, that the transitional eigenvalues go to zero quite fast and cannot be expected to produce a noticeably better resolution in the reconstructions. In the case of the homogeneous model 2, which is illustrated

in Figs. 11(c) and 11(d) for comparison, the transition region is almost absent or, at least, it is consistent with that of an irregular DFT [56].

In practice, what matters for determining whether an eigenvalue is significant or insignificant is not its absolute magnitude but the ratio to the largest eigenvalue in the spectrum. The dynamic range of values displayed in Fig. 11(a) is very large, i.e., $\gtrsim 10^{15}$. In a realistic reconstruction, only a few of the transitional eigenvalues (with the associated eigenvectors), if any at all, carry useful information about the target. In the presence of experimental noise, most of these modes will be suppressed. So the overall improvement of the nonlinear reconstruction compared to the linearized one in terms of well-posedness of inversion will hardly be noticeable.

We illustrate the above point further in Fig. 12 where we plot the spectra of W[D] normalized to the largest eigenvalue and compare various interactions G. In addition to the Green's function of the three-dimensional wave equation (55), we adduce in Fig. 12 results the tight-binding interaction $G_{nm} = g(1 + 0.1i)(\delta_{n,m-1} + \delta_{n,M+1})$ (also used in Appendix A) and the fully connecting interaction of Secs. III, IV, $G_{nm} = g(1 + 0.1i)(1 - \delta_{nm})$. The factor $1 + 0.1i$ is introduced to avoid numerical instability in computing S[D] (that is, to make sure that the forward problem has a numerically stable solution). In the case of fully connecting interactions, the transition from significant to insignificant eigenvalues is perfectly sharp (up to the finite precision of the computer) and occurs exactly at $n = 4L + 1 = 205$, as was proved theoretically in Sec. IV. For the other two interactions, a transition region exists but is insignificant. We therefore conclude that the fully connecting interaction is a reasonable model for examining uniqueness of solutions to nonlinear ISPs.

We now turn to the case when the linearized ISP is not band-limited. This corresponds to $L = 650$; the eigenvalues
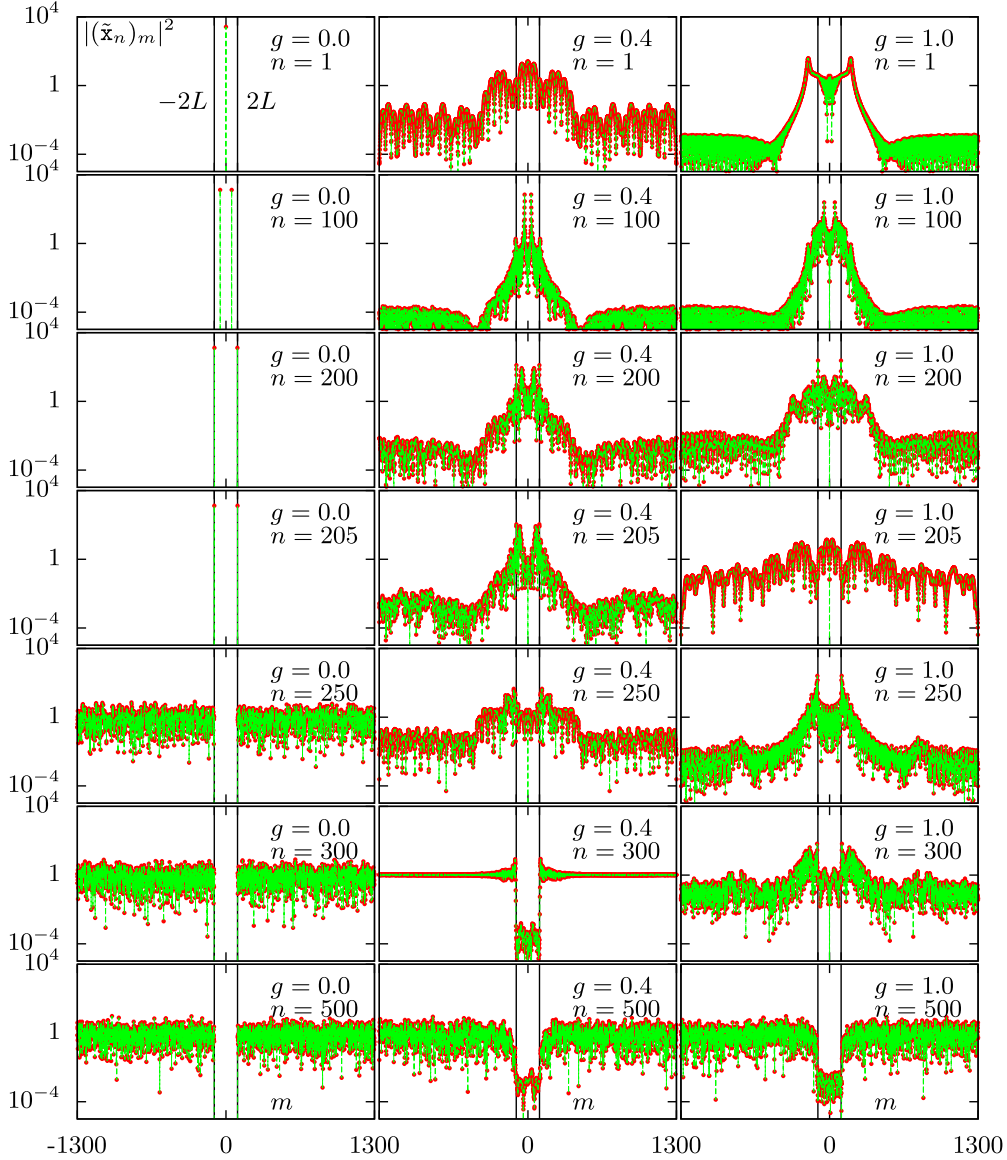
FIG. 13. Squared components of the Fourier-transformed eigenvectors $\tilde{x}_n[D]$ as functions of the component index m for various parameters as labeled. The matrix $W[D]$ is computed for model 1. Solid vertical lines are drawn at $m = \pm 2L = \pm 102$. The data points are represented by filled red circles and the dashed green lines are shown to guide the eye.

of $W[D]$ for this L are illustrated in Figs. 11(b) and 11(d). It is evident that in this case there is no gap in the spectrum and all eigenvalues remain significant regardless of g. The apparent precipitous drop of $w_n[D]$ near the right bound of the plots is, in fact, fully consistent with the linear decrease due to the change in statistical weights of $w_n[D]$, as discussed above. If plotted using a linear scale on all axes, the dependence near the right edge of the plots will appear as linear. No numerically small (insignificant) eigenvalues are present in the data sets of Figs. 11(b) and 11(d). This means that the solution to the nonlinear ISP remains unique if the solution to the corresponding linearized ISP is unique. However, the condition number of $W[D]$ tends to increase with g. This is due to the resonance phenomena discussed above. A closely related observation is the existence of surfaces of discontinuity in the inverse solution to the nonlinear ISP. Linearization at the points that are close to a discontinuity can result in matrices

$W[D]$ with very large condition numbers. A one-dimensional analogy is when a function $f(x)$ is locally invertible near x_0 but the derivative $f'(x_0)$ is very large. This can happen if $f(x)$ has a discontinuity at x_1, which is close to x_0.

Next, we look more closely at the eigenvectors of $W[D]$. Let x_n be the set of orthonormal eigenvectors so $W[D]x_n[D] = w_n[D]x_n[D]$. Each $x_n[D]$ is a vector of length N with the components $(x_n[D])_j$. The eigenvalues are assumed to be arranged in descending order so $w_{max}[D] = w_1[D]$. We can define the Fourier transforms of $x_n[D]$ as

$$(\tilde{x}_n[D])_m = \sum_{j=1}^{N} (x_n[D])_j e^{i\xi m j}, \tag{63}$$

where $-M \leqslant m \leqslant M$, $M = (N-1)/2$. In Fig. 13, we plot the squared components of $(\tilde{x}_n[D])_m$ as functions of m for $L = 51$, D given by model 1, different g, and different eigenvalue
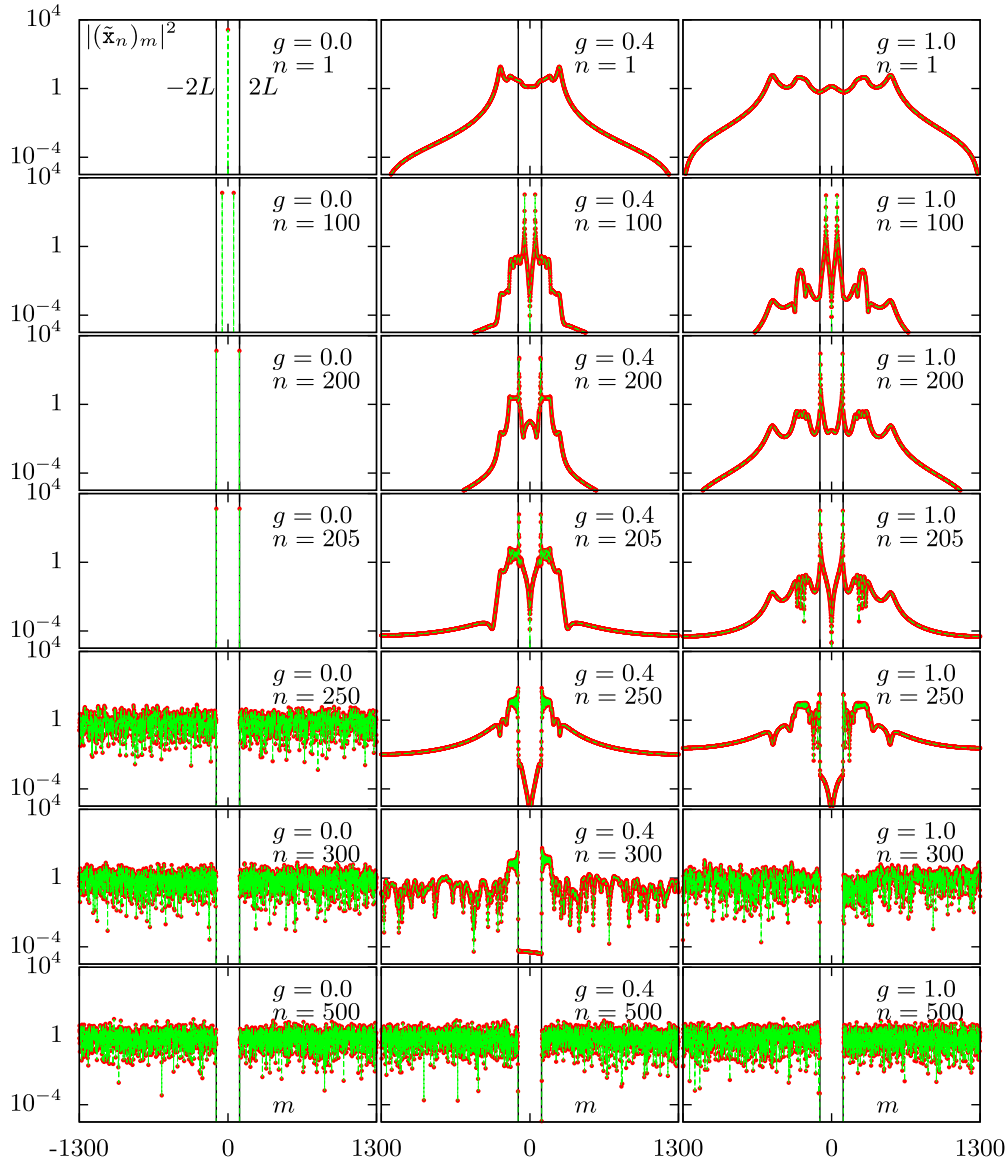
FIG. 14. Same as in Fig. 13 but for D given by model 2 (D = I).

indexes n. Note that the Fourier coefficients $(\tilde{x}_n[D])_m$ with $-2L \leqslant m \leqslant 2L$ lie within the band limit. The special values $m = \pm 2L$ are shown in Fig. 13 by two vertical lines.

In the case $g = 0$ (left column of images in Fig. 13), the first $4L + 1 = 205$ eigenvectors correspond to significant (nonzero) eigenvalues. Projection of α onto these eigenvectors can be computed by solving the linearized ISP. The eigenvectors with $n > 4L + 1$ have zero eigenvalues. It can be seen that all significant eigenvectors are band limited in the sense that they have nonzero Fourier coefficients only within the band limit $-2L \leqslant m \leqslant 2L$. The insignificant eigenvectors (those with $n > 4L + 1$) do not have any nonzero components within the band limit. This is all consistent with the standard Fourier analysis of the linearized ISP. When we move to the cases $g = 0.4$ (middle column of images) and $g = 1.0$ (right column of images), the consideration is no longer that simple. It can be seen that the significant eigenvectors have nonzero components both within and outside of the band limit. Same is true for the transition eigenvectors, i.e., for the index $n = 250$.

The Fourier coefficients of insignificant eigenvectors (i.e., $n = 500$) can also be nonzero both inside and outside of the band limit, although those that are outside visibly dominate. We can conclude that for $g > 0.4$ and $g = 1.0$, the number of significant eigenvectors is approximately the same as in the case $g = 0$ (or slightly larger due to the existence of transitional eigenvalues) but is still smaller than the number of nonzero Fourier coefficients in these vectors. Therefore, projecting $\tilde{\alpha}$ onto the significant eigenvectors of W[D] does not generate enough equations to find $\tilde{\alpha}$ or any of its components with confidence.

In Fig. 14, we display the squared coefficients $(\tilde{x}_n[D])_m$ for D = I (model 2). Basically, the same conclusions can be drawn. In the cases when $g > 0$, the significant eigenvectors couple together more Fourier coefficients $(\tilde{x}_n[D])_m$ than the number of significant eigenvectors themselves. Therefore, there are not enough equations to find any of these components reliably. The insignificant eigenvectors are however localized outside of the band limit stronger than for model 1.

Overall, the situation is very similar to what we have observed in Sec. IV. Namely, if the linearized ISP is ill-posed, the nonlinear ISP remains ill-posed and contains, essentially, the same number of significant equations. However, when $g = 0$, only the Fourier coefficients $\tilde{\alpha}_m$ within the band limit are coupled to the data so there are enough equations to find these coefficients reliably, while the coefficients outside of the band limit are fundamentally unknown. In the case of $g \neq 0$, the number of significant equations remains the same but now *all* Fourier coefficients $\tilde{\alpha}_m$ become coupled to the data so *none* of them can be computed reliably. The geometrical interpretation of this phenomenon is that the linear subspace of solutions that is characteristic of the $g = 0$ limit becomes a curved manifold when $g \neq 0$. An example of such manifolds is graphically illustrated in Sec. III.

VII. DISCUSSION

We have considered the question whether solving a nonlinear ISP can provide super-resolution in the situations wherein the linearized ISP is band limited. A number of examples suggest that this kind of super-resolution does not exist in a practical sense. Essentially, we have provided several counterexamples to the conjecture of super-resolution by solving a nonlinear ISP.

The approach based on counterexamples can, of course, be criticized as not sufficiently general. In particular, we have so far considered only one-dimensional targets. However, there are grounds to believe that the provided examples are indicative of a more general tendency. In particular, we have shown in Sec. VI C (Fig. 12) that there is not much qualitative difference between the cases of the fully connecting interaction, tight-binding interaction and the realistic interaction given by the Green's function of the three-dimensional wave equation. While in the case of the fully connecting interaction, the transition from significant to insignificant eigenvalues is perfectly sharp, as was proved theoretically in Sec. IV, there is some narrow transition region for the other two interactions. The transition eigenvalues observed in the latter two cases can be interpreted as additional mathematically independent equations of the form described theoretically in Appendix A 2. However, the transition regions are narrow and the eigenvalues drop down precipitously. Therefore, we conclude that the fully connecting interaction is a reasonable model to investigate the effects of super-resolution in nonlinear ISPs. But, for the fully connecting interaction, the ISP can be solved analytically for any geometry or dimensionality of the target. The results of Sec. IV can be generalized to three dimensional targets without conceptual difficulty, although this entails working with irregular DFTs. Moreover, the one-dimensional targets considered in this paper can be viewed as being embedded in the three-dimensional space and, therefore, they are special cases of more general three-dimensional targets. If there is no super-resolution for these relatively simple targets, one can hardly expect super-resolution to emerge for more complicated objects.

We thus conclude that the effect of nonlinearity is not to force uniqueness of inverse solutions but, rather, to transform a linear subspace of possible solutions into a more general curved manifold. This tendency is already manifest in the simplest toy problem with three degrees of freedom that was discussed in Sec. III; examples of such manifolds are graphically illustrated in Fig. 1. Moreover, as the strength of nonlinearity is increased, the reconstruction become more sensitive to noise. This tendency is present even if complete data are available and the inverse solution is unique, as is illustrated in Fig. 6 above.

Finally, a comment on the existing demonstrations of super-resolution needs to be made. For example, in Ref. [19], a resolution of $\sim\lambda/10$ was demonstrated by solving a nonlinear ISP. However, this result was obtained only after using a strong *a priori* constraint on the possible values that the unknown contrast can take. We believe that such constraints can be crucial and indeed result in super-resolution either in linearized or full nonlinear ISPs. Of course, if the ISP is essentially nonlinear, it should not be linearized, lest the inverse solution turns out to be useless, either with the constraints or not. It is the combination of solving the correctly stated nonlinear ISP and the use or prior information that allowed achieving the $\lambda/10$ resolution in Ref. [19]. In this paper, we assumed no prior information about the target. An interplay of nonlinearity of the ISP and the use of *a priori* constraints on the target is an interesting direction for further research.

APPENDIX: EXAMPLE WITH FOUR DEGREES OF FREEDOM

In this Appendix, we analyze the problem with four degrees of freedom quantified by the polarizabilities $\alpha = [\alpha_1, \alpha_2, \alpha_3, \alpha_4]^{\mathrm{T}}$. We will consider two different tight-binding interaction $\mathtt{G}$ as detailed below. One form of interaction will be cyclic, that is, it will correspond to a closed loop (simply, a square) of particles, and the other will correspond to an open chain. The model is exactly solvable in both cases although, for the open chain, the solution is very involved. We will show that, depending on the choice of interaction, accounting for the ISP nonlinearity may or may not provide one additional mathematically independent equation and thus render the inverse solution unique.

In both cases, we will use the following three basis vectors to construct the measurement matrices $\mathtt{A}$ and $\mathtt{B}$:

$$\mathtt{u} = \begin{bmatrix} 1 \\ 1 \\ 1 \\ 1 \end{bmatrix}, \quad \mathtt{v} = \begin{bmatrix} 1 \\ -1 \\ 1 \\ -1 \end{bmatrix}, \quad \mathtt{w} = \begin{bmatrix} 1 \\ 0 \\ -1 \\ 0 \end{bmatrix}, \quad (A1)$$

so

$$A = \begin{bmatrix} 1 & 1 & 1 & 1 \\ 1 & -1 & 1 & -1 \\ 1 & 0 & -1 & 0 \end{bmatrix}, \quad B = \begin{bmatrix} 1 & 1 & 1 \\ 1 & -1 & 0 \\ 1 & 1 & -1 \\ 1 & -1 & 0 \end{bmatrix}. \quad (A2)$$

Accounting for the symmetry of Φ, the problem involves six data points ϕ_{11}, ϕ_{12}, ϕ_{13}, ϕ_{22}, ϕ_{23}, and ϕ_{33} and four unknowns.

Therefore, at least two of the above data points are not independent but related to the rest by the physical admissibility conditions.

The linearized ISP for the setup considered in this Appendix is band limited. The subspace of solutions to (18) with the measurement matrices (A2) is defined by

$$\alpha_1^{\text{inv}} = \tfrac{1}{2}(\phi_{33} + \phi_{23}), \tag{A3a}$$

$$\alpha_3^{\text{inv}} = \tfrac{1}{2}(\phi_{33} - \phi_{23}), \tag{A3b}$$

$$\alpha_2^{\text{inv}} + \alpha_4^{\text{inv}} = \phi_{22} - \phi_{33}. \tag{A3c}$$

The physical admissibility conditions in the linear regime consist of the three equations:

$$\phi_{13} = \phi_{23}, \quad \phi_{12} + \phi_{22} = 2\phi_{33}, \quad \phi_{11} = \phi_{22}. \tag{A3d}$$

1. Cyclic tight-binding interaction

Consider the case when G is given by

$$\mathsf{G} = \begin{bmatrix} 0 & g & 0 & g \\ g & 0 & g & 0 \\ 0 & g & 0 & g \\ g & 0 & g & 0 \end{bmatrix}. \tag{A4}$$

This interaction can be interpreted as a tight-binding model for four particles arranged in the vertices of a square. Any two particles connected by a square side interact with the strength g but the pairs of particles connected by the square diagonals do not interact. In this case, the solution to the nonlinear ISP is still not unique. The set of possible solutions is defined by

$$\alpha_1^{\text{inv}} = \frac{1}{2} \frac{(\phi_{12} + \phi_{22})\phi_{33} - (\phi_{13} + \phi_{23})\phi_{23}}{\phi_{12} + \phi_{22} - 2\phi_{33}},$$

$$\alpha_3^{\text{inv}} = \frac{1}{2} \frac{(\phi_{12} + \phi_{22})\phi_{33} - (\phi_{13} + \phi_{23})\phi_{23}}{\phi_{12} + \phi_{22} + 2\phi_{33}},$$

$$\alpha_2^{\text{inv}} + \alpha_4^{\text{inv}}$$
$$= \frac{\phi_{13}(\phi_{22} - \phi_{23}) + \phi_{23}(\phi_{23} - \phi_{12}) + \phi_{33}(\phi_{12} - \phi_{22})}{\phi_{12} + \phi_{13} + \phi_{22} - 4\phi_{33} + 2g(\phi_{22}\phi_{33} - \phi_{23}^3)},$$

and the physical admissibility conditions consist of the following three equations:

$$\frac{\phi_{13}}{\phi_{23}} = \frac{1 + g(\phi_{22} - 3\phi_{33}) + g^2(\phi_{22}\phi_{33} - \phi_{23}^2)}{1 - g\phi_{22} - g^2\phi_{23}^2 - g\phi_{33} + g^2\phi_{22}\phi_{33}},$$

$$\phi_{12} = \frac{2\phi_{33} - \phi_{22} + g(\phi_{23}^2 - \phi_{22}\phi_{33} - \phi_{13}\phi_{23})}{1 - g\phi_{33}},$$

$$\phi_{11}(\phi_{22} - \phi_{33}) = \phi_{12}^2 - \phi_{13}^2$$
$$+ \phi_{23}(2\phi_{13} - \phi_{23}) + \phi_{33}(\phi_{22} - 2\phi_{12}).$$

It is interesting to note that this solution describes a linear subspace rather than a curved manifold. This is a consequence of the special measurement scheme considered here. It happens so the forward equations contain the combination $\alpha_2 + \alpha_4$ and not α_2 or α_4 individually. By using various subsets of the basis vectors in (A1) and the fourth basis vector, $[0, 1, 0, -1]^{\text{T}}$, for constructing the measurement matrices A and B, one can create a linear subspace of solutions in which $\alpha_2 + \alpha_4$ is replaced by any pairwise sum $\alpha_i + \alpha_j$ with $i \neq j$. All these inverse

solutions are nonlinear in the data and therefore experience discontinuities.

2. Noncyclic tight-binding interaction

Next, let G be given by

$$\mathsf{G} = \begin{bmatrix} 0 & g & 0 & 0 \\ g & 0 & g & 0 \\ 0 & g & 0 & g \\ 0 & 0 & g & 0 \end{bmatrix}. \tag{A5}$$

This interaction corresponds to a linear open chain of four particles with nearest-neighbor interactions. Even though the interaction (A5) appears to be simpler than (A4), it results in a very complicated nonlinear inverse solution. Generally, we can write

$$\alpha_k^{\text{inv}} = f_k(g; \phi_{11}, \phi_{22}, \phi_{23}, \phi_{33}), \quad k = 1, 2, 3, 4, \tag{A6}$$

where $f_k(\cdot)$ are single-valued functions defined for $g \neq 0$ except at some surfaces of discontinuity. Thus, the nonlinear inverse solution in this case is unique, unlike its linearized counterpart. The complete inverse solution is quite complicated and given below in Appendix A 3. However, the first two leading terms in the expansions of α_k^{inv} in powers of g are relatively simple and given by the following expressions:

$$\alpha_1^{\text{inv}} = \frac{1}{8}(\phi_{11} - \phi_{22}) + \frac{1}{2}(\phi_{33} + \phi_{23})$$
$$+ \frac{g}{8}\Big[\phi_{22}(\phi_{11} - \phi_{22} + 4\phi_{23})$$
$$+ \phi_{33}(4\phi_{33} - 4\phi_{23} - 3\phi_{11} - \phi_{22})\Big] + O(g^2), \tag{A7a}$$

$$\alpha_2^{\text{inv}} = \frac{2}{g} \frac{\phi_{11} - \phi_{22}}{\phi_{11} - \phi_{22} + 4(\phi_{23} + \phi_{33})}$$
$$+ \frac{\phi_{11} - \phi_{22} + 4(\phi_{23} - \phi_{33})}{(\phi_{11} - \phi_{22} + 4(\phi_{23} + \phi_{33}))^2}$$
$$\times \Big[\phi_{22}^2 + \phi_{22}(2\phi_{23} + \phi_{33}) - \phi_{11}(\phi_{22} - 2\phi_{23} - 3\phi_{33})$$
$$- 4\phi_{33}(\phi_{23} + \phi_{33})\Big] + O(g^1), \tag{A7b}$$

$$\alpha_3^{\text{inv}} = \frac{1}{8}(\phi_{22} - \phi_{11}) + \frac{1}{2}(\phi_{33} - \phi_{23})$$
$$- \frac{g}{32}(3\phi_{11} + \phi_{22} - 4\phi_{33})$$
$$\times (\phi_{11} - \phi_{22} + 4\phi_{23} - 4\phi_{33}) + O(g^2), \tag{A7c}$$

$$\alpha_4^{\text{inv}} = \frac{2}{g} \frac{\phi_{22} - \phi_{11}}{\phi_{11} - \phi_{22} + 4(\phi_{23} + \phi_{33})}$$
$$+ \frac{2}{(\phi_{11} - \phi_{22} + 4(\phi_{23} + \phi_{33}))^2}$$
$$\times \Big[\phi_{22}(\phi_{11} - \phi_{22})(\phi_{11} - \phi_{22} + 4\phi_{23}) + 4\phi_{23}\phi_{33}$$
$$\times (\phi_{11} + 3\phi_{22}) + 8\phi_{33}^2(\phi_{11} + \phi_{22} - 2(\phi_{23} + \phi_{33}))$$
$$- \phi_{33}(\phi_{11} - \phi_{22})^2\Big] + O(g^1). \tag{A7d}$$

In addition, there are two equations of physical admissibility of the data matrix. These conditions can be defined implicitly by expressing ϕ_{12} and ϕ_{13} in terms of $\alpha_1, \alpha_2, \alpha_3,$ and α_4 and then using the complete inverse solutions given in

Sec. A 3 to express α_k in terms of ϕ_{11}, ϕ_{22}, ϕ_{23}, and ϕ_{33}. These conditions are very complicated and not stated here explicitly.

An important observation that we can make is that the inverse solutions (A7a), (A7c) for α_1 and α_3 approach the linearized solutions (A3a), (A3b) when $g \to 0$ [accounting for the physical admissibility condition (A3d)]. However, this is not so for the inverse solutions (A7b), (A7d) for α_2 and α_4. If the data are ideal, (A7b), (A7d) have well-defined limits when $g \to 0$ and it should not matter how g approaches zero in the complex plane. However, the solutions cannot be obtained by formally setting $g = 0$ because the perturbation theory in g (for the inverse solutions) is singular.

The unique inverse solution described above is an example of super-resolution that is obtained purely due to accounting for the ISP nonlinearity; it cannot be obtained by formally setting $g = 0$ and considering the linearized ISP. In a more general context, the mathematical question is whether a singular perturbation theory that leads to the solutions of the kind (A7) is possible, numerically stable, and how many additional equations (degrees of freedom) it allows us to fix. Perturbative investigation of the inverse solutions (keeping in mind that the perturbation is singular and can lead to Laurent series expansions) is a promising avenue of research but we do not follow it here. Instead, we present below a number of numerical examples in which the question can be addressed nonperturbatively and show that, for large systems and realistic interactions, the number of additional degrees of freedom that can be recovered by accounting for the nonlinearity is practically insignificant.

3. Analytical solution for the four-particle chain problem

Here we state the complete analytical solution to the inverse problem stated in Appendix A 2. Considering the upper triangle of the matrix equation $\mathtt{A}[\mathtt{I} - \mathtt{VG}]^{-1}\mathtt{VB} = \Phi$, we can write explicitly six nonlinear equations for four unknowns. Obviously, not all these equations are independent. Assuming the data matrix is in range of the forward operator (as we say, is *physically admissible*), the inverse solution can be written in terms of the following elements of the data matrix: ϕ_{11}, ϕ_{22}, ϕ_{23} and ϕ_{33}. The remaining two matrix elements, ϕ_{12} and ϕ_{13}, are not mathematically-independent from the former four elements. For economy of writing, we use below the following shorthand notations:

$$\lambda = \phi_{11}, \quad \mu = \phi_{22}, \quad \nu = \phi_{23}, \quad \xi = \phi_{33}.$$

Then

$$\alpha_k^{\mathrm{inv}} = \frac{\mathcal{N}_k}{g\mathcal{D}_k}, \quad k = 1, 2, 3, 4,$$

where

$$\mathcal{N}_k = a_k + b_k g + c_k g^2 + d_k g^3 + e_k g^4,$$
$$\mathcal{D}_k = p_k + q_k g + r_k g^2 + s_k g^3 + t_k g^4.$$

The coefficients are given by the following expressions:

$a_1 = 2(1 - R)$;

$b_1 = 2[\lambda + 8\nu + 7\xi - 2\mu + (3\xi - \nu)R]$;

$c_1 = \lambda(6\nu - \mu - \xi) + \mu(\mu - 12\nu - 19\xi) + 28\nu^2$
$\quad + 2\xi(5\nu - 6\xi) + 2[\nu(2\xi + \nu) - \xi(2\xi + \mu)]R$;

$d_1 = 2[\lambda(3\nu^2 - \mu\nu - \mu\xi - \nu\xi) + \nu(8\nu^2 - 3\nu\xi - 2\xi^2)$
$\quad + \mu(\mu\nu + 4\mu\xi + 7\xi^2 - 9\nu\xi - 6\nu^2)$
$\quad + (\mu\xi^2 + \nu^3 - \nu^2\xi - \mu\nu\xi)R]$;

$e_1 = \lambda\mu(\xi^2 + \mu\xi - 2\nu\xi - \nu^2) + \nu\xi(4\mu^2 - \lambda\nu - 2\nu^2)$
$\quad + \mu\nu(\nu\xi + 2\xi^2 + \mu\nu - 4\nu^2) - \mu^2\xi(3\xi + \mu)$
$\quad + 2\nu^3(\lambda + \nu)$;

$p_1 = 32$;

$q_1 = 8(\lambda + 8\nu - 4\xi - 5\mu)$;

$r_1 = 8(\xi + 2\mu - 2\nu - \lambda)(\mu + \xi - 2\nu)$;

$s_1 = 2(\lambda - \mu)(\mu + \xi - 2\nu)^2$;

$t_1 = 0$;

$a_2 = 2[\lambda - \mu + 2(\nu + \xi) - 2(\nu + \xi)R]$;

$b_2 = \lambda(6\nu - \mu - \xi) + \mu(\mu - 6\nu - 11\xi) + 8\xi^2 + 4\nu^2$
$\quad + 4(\xi^2 + \mu\xi - 2\nu^2)R$;

$c_2 = 2[\lambda(3\nu^2 - \mu\nu - \mu\xi - \nu\xi) + \mu(\mu\nu + 3\mu\xi$
$\quad - 3\nu^2 - 3\nu\xi) + 2\nu(\nu\xi + 3\xi^2 - \nu^2) - 4\xi^3$
$\quad + 2(\xi - \nu)(\nu^2 - \mu\xi)R]$;

$d_2 = (\mu\xi - \nu^2)$
$\quad \times [4(\nu - \xi)^2 + \mu(2\nu - \xi) + \lambda(\mu - 2\nu + \xi) - \mu^2]$;

$e_2 = 0$;

$p_2 = \lambda - \mu + 4(\nu + \xi)$;

$q_2 = 4\nu(\lambda + 4\nu - \mu) + 8(3\nu - \mu)\xi + 16\xi^2$;

$r_2 = 2[3\nu^2(\lambda + 4\nu - \mu) + \xi(\mu^2 - \lambda\mu + 16\nu^2 - 12\mu\nu)$
$\quad - 8\xi^2(\mu + \xi)]$;

$s_2 = 4(\nu^2 - \mu\xi)[\nu(\lambda + 4\nu - \mu) + 2\xi(\nu - \mu) - 4\xi^2]$;

$t_2 = (\lambda - \mu + 4\nu - 4\xi)(\nu^2 - \mu\xi)^2$;

$a_3 = 2(R - 1)$;

$b_3 = \lambda + \mu - 2\nu$;

$c_3 = d_3 = e_3 = 0$;

$p_3 = 8$;

$q_3 = 2(\lambda - \mu)$;

$r_3 = s_3 = t_3 = 0$;

$a_4 = 2[\mu - \lambda - 2(\nu + \xi) + 2(\nu + \xi)R]$;

$b_4 = 2[\lambda(\mu - 2\nu + \xi) + \mu(4\nu - \mu) + \xi(7\mu + 2\nu - 4\xi)$
$\quad + 2(\nu^2 - 2\xi^2 - \xi(\mu + 2\nu))R]$;

$c_4 = 4[\lambda\nu(\mu + \xi) + \mu(3\nu^2 + 3\nu\xi + 3\xi^2) - \mu^2(\nu + 3\xi)$
$\quad + \nu(2\nu^2 - 3\nu\xi - 6\xi^2) + (\mu\xi(\nu + 3\xi) - \nu^2(\nu + 3\xi))R]$;

$d_4 = 2[(\mu\xi - \nu^2)(\mu^2 - \lambda(\mu + 2\nu + \xi) + 10\nu\xi$
$\quad - \mu(4\nu + 3\xi) + 2(\nu^2 - \mu\xi)R)]$;

$$e_4 = 2(\lambda + \mu - 2\nu)(\nu^2 - \mu\xi)^2;$$

$$p_4 = \lambda - \mu + 4(\nu + \xi);$$

$$q_4 = 4(\nu(\lambda - \mu + 4\nu) - 2(\mu - 3\nu)\xi + 4\xi^2);$$

$$r_4 = 2[3\nu^2(\lambda + 4\nu - \mu) + \xi(16\nu^2 + \mu^2) - \mu\xi(12\nu + \lambda)$$
$$- 8\xi^2(\mu + \xi)];$$

$$s_4 = 4(\nu^2 - \mu\xi)[\nu(\lambda - \mu + 4\nu) + 2\xi(\nu - \mu) - 4\xi^2];$$

$$t_4 = (\lambda - \mu + 4\nu - 4\xi)(\nu^2 - \mu\xi)^2.$$

In these expressions,

$$R = [1 - 2g(\lambda + \nu - 2\xi)$$
$$+ g^2(\nu^2 - \mu\xi + \lambda\mu - 2\lambda\nu + \lambda\xi)]^{1/2}.$$

The square root branch is defined by the conventional condition $-\pi/2 < \arg(\sqrt{z}) \leqslant \pi/2$. Strictly speaking, the nonlinear forward equations have two solutions, one with $+R$ and the other with $-R$. However, only the solution defined above has the same $g \to 0$ limit for α_1^{inv}, α_3^{inv} as the linearized solution (A3). The second branch produces a solution in which $\alpha_1^{\text{inv}}, \alpha_3^{\text{inv}} = O(g^{-1})$ when $g \to 0$. This solution can be viewed as belonging to the "remote" manifold. Similar remote manifolds may appear even if there are no square roots or other multivalued functions involved; a similar occurrence is illustrated in Fig. 1 where emergence of the remote manifold can be explained by the inverse solution discontinuity (in the data).

More generally, the small-g asymptotes of the solution stated in this Appendix (with the square root convention mentioned above) are given in (A7).

[1] K. Nasrollahi and T. B. Moeslund, Machine Vision Appl. **25**, 1423 (2014).

[2] Y. Romano, M. Elad, and M. Peyman, SIAM J. Imag. Sci. **10**, 1804 (2017).

[3] D. Rajan and S. Chaudhuri, Image Vision Comput. **19**, 957 (2001).

[4] C. V. Jiji, P. Neethu, and S. Chaudhuri, in *Compute Vision—ECCV 2006*, edited by A. Leonardis, H. Bischof, and A. Pinz (Springer, Berlin Heidelberg, New York, 2006), pp. 255–266.

[5] D. Watzenig, Elektrotech. Inftech. **124**, 240 (2007).

[6] R. L. Lagendijk and J. Biemond, *Iterative Identification and Restoration of Images* (Springer, New York, 1991).

[7] X. Liu, D. Zhai, D. Zhao, G. Zhai, and W. Gao, IEEE Trans. Imag. Proc. **23**, 1491 (2014).

[8] L. I. Rudin, S. Osher, and E. Fatemi, Physica D **60**, 259 (1992).

[9] A. Beck and M. Teboulle, SIAM J. Imag. Sci. **2**, 183 (2009).

[10] J. A. Tropp and A. C. Gilbert, IEEE Trans. Info. Theor. **53**, 4655 (2007).

[11] T. Blumensath, Sign. Proc. **92**, 752 (2012).

[12] T. Blumensath, IEEE Trans. Info. Theor. **59**, 3466 (2013).

[13] M. Nieto-Vesperinas, J. Opt. Soc. Am. A **21**, 491 (2004).

[14] N. A. Kuhta, V. A. Podolskiy, and A. L. Efros, Phys. Rev. B **76**, 205102 (2007).

[15] F. Simonetti, Phys. Rev. E **73**, 036619 (2006).

[16] K. Belkebir, P. C. Chaumet, and A. Sentenac, J. Opt. Soc. Am. A **23**, 586 (2006).

[17] G. Maire, F. Drsek, J. Girard, H. Giovannini, A. Talneau, D. Konan, K. Belkebir, P. C. Chaumet, and A. Sentenac, Phys. Rev. Lett. **102**, 213905 (2009).

[18] C. Gilmore, P. Mojabi, A. Zakaria, S. Pistorius, and J. LoVetri, IEEE Antennas Wireless Propagation Lett. **9**, 393 (2010).

[19] T. Zhang, C. Godavarthi, P. C. Chaumet, G. Maire, H. Giovannini, A. Talneau, M. Allain, K. Belkebir, and A. Sentenac, Optica **3**, 609 (2016).

[20] M. Born and E. Wolf, *Principles of Optics* (Cambridge University Press, Cambridge, UK, 1999).

[21] P. S. Carney and J. C. Schotland, Appl. Phys. Lett. **77**, 2798 (2000).

[22] P. S. Carney, V. A. Markel, and J. C. Schotland, Phys. Rev. Lett. **86**, 5874 (2001).

[23] P. S. Carney and J. C. Schotland, J. Opt. Soc. Am. A **20**, 542 (2003).

[24] J. Sun, P. S. Carney, and J. C. Schotland, IEEE J. Sel. Top. Quantum Electron. **12**, 1072 (2006).

[25] J. Sun, J. C. Schotland, R. Hillenbrand, and P. S. Carney, Appl. Phys. Lett. **95**, 121108 (2009).

[26] V. A. Markel, V. M. Shalaev, P. Zhang, W. Huynh, L. Tay, T. L. Haslett, and M. Moskovits, Phys. Rev. B **59**, 10903 (1999).

[27] Z. Ulanowski, A. Wang, P. H. Kaye, and I. K. Ludlow, Appl. Opt. **37**, 4027 (1998).

[28] V. V. Berdnik, K. Gilev, A. Shvalov, V. Maltsev, and V. A. Loiko, J. Quant. Spectrosc. Radiat. Transfer **102**, 62 (2006).

[29] A. V. Romanov, A. I. Konokhova, E. S. Yastrebova, K. V. Gilev, D. I. Strokotov, A. V. Chernyshev, V. P. Maltsev, and M. A. Yurkin, J. Quant. Spectrosc. Radiat. Transfer **200**, 280 (2017).

[30] A. Corlu, R. Durduran, R. Choe, M. Schweiger, E. Hillman, S. Arridge, and A. Yodh, Appl. Opt. **44**, 2082 (2005).

[31] B. Deutsch, R. Reddy, D. Mayerich, H. Bhagrava, and P. S. Carney, J. Opt. Soc. Am. A **32**, 1126 (2015).

[32] J. Sylvester and G. Uhlmann, Ann. Math. **125**, 153 (1987).

[33] R. G. Newton, *Scattering Theory of Waves and Particles* (McGraw-Hill, New York, 1966).

[34] A. Gonis, *Green Functions for Ordered and Disordered Systems* (Elsevier, New York, 1992).

[35] M. Moghaddam, W. C. Chew, and M. Oristaglio, Int. J. Imaging Syst. Technol. **3**, 318 (1991).

[36] M. Moghaddam and W. C. Chew, IEEE Trans. Geosci. Remote Sensing **30**, 147 (1992).

[37] F.-C. Chen and W. C. Chew, Appl. Phys. Lett. **72**, 3080 (1998).

[38] T. J. Cui, W. C. Chew, X. X. Yin, and W. Hong, IEEE Trans. Antennas Propag. **52**, 1398 (2004).

[39] J. de Rosny and C. Prada, Phys. Rev. E **75**, 048601 (2007).

[40] F. Simonetti, Phys. Rev. E **75**, 048602 (2007).

[41] M. T. Testorf and M. A. Fiddy, Adv. Imaging Electron Phys. **163**, 165 (2010).

[42] A. A. Maznev and O. B. Wright, Wave Motion **68**, 182 (2017).

[43] H. W. Levinson and V. A. Markel, Phys. Rev. E **94**, 043318 (2016).

[44] V. A. Markel, J. Quant. Spectrosc. Radiat. Transfer **236**, 106611 (2019).

[45] L. L. Foldy, Phys. Rev. **67**, 107 (1945).

[46] M. Lax, Rev. Mod. Phys. **23**, 287 (1951).

[47] V. A. Markel, J. Mod. Opt. **40**, 2281 (1993).

[48] E. M. Purcell and C. R. Pennypacker, Astrophys. J. **186**, 705 (1973).

[49] B. T. Draine, Astrophys. J. **333**, 848 (1988).

[50] In Ref. [44], the local and the incident fields are denoted by e_n and E_n, respectively. Here we use a different convention (small letter is reserved for the incident field) to achieve a uniformity of notations, so all vectors are denoted by small letters and matrices are denoted by capital letters.

[51] Here we used the fact that the basis vectors are real. In the more general case, A and B would be Hermitian conjugates (adjoints) of each other.

[52] The equality here is approximate because the derivation of (50) involved a first-order approximation in V. The solution can be iteratively improved by a straightforward application of the Newton's method.

[53] The inverse DFT only uses a subset of equations in (18). While, in the ideal case, these equations are redundant, in practice they correspond to different physical measurements and can have different right-hand sides due to the experimental noise. To use the DFT, one needs to decide which particular equation (and which corresponding measurement) to keep; the rest are discarded. The pseudoinverse solution described in Sec. VI B utilizes all equations in (18) so statistical averaging of noise can be achieved.

[54] H. Lev-Ari, Comm. Inform. Sys. **5**, 123 (2005).

[55] V. A. Markel, H. Levinson, and J. C. Schotland, Inverse Problems **35**, 124002 (2019).

[56] While there exists vast literature on discrete Fourier transforms of nonuniformly spaced data, we did not find any results nor discussion of the singular values transition region for band-limited transforms. The statements made in this paper are based on the author's own simulations.